ALMA MATER STUDIORUM
UNIVERSITY OF BOLOGNA
SCHOOL OF ENGINEERING AND ARCHITECTURE
Master of Science Degree in Aerospace Engineering

Testing of subgrid scale (SGS) models for large-eddy simulation (LES) of turbulent channel flow

Master thesis in Applied Aerodynamics

SUPERVISORS:
Prof. Alessandro Talamelli
Prof. Arne V. Johansson

STUDENT:
Matteo Montecchia

ASSISTANT SUPERVISOR:
Dr. Geert Brethouwer

Academic Year 2013-2014
Session III

Your work is going to fill a large part of your life,
and the only way to be truly satisfied
is to do what you believe is great work.
And the only way to do great work
is to love what you do.
If you haven't found it yet, keep looking.
Don't settle.
As with all matters of the heart, you'll know when you find it.
Steve Jobs

"Vedi caro amico cosa ti scrivo e ti dico
e come sono contento
di essere qui in questo momento,
vedi caro amico cosa si deve inventare
per poterci ridere sopra,
per continuare a sperare."

Abstract

Sub-grid scale (SGS) models are required in order to model the influence of the unresolved small scales on the resolved scales in large-eddy simulations (LES), the flow at the smallest scales of turbulence.

In the following work two SGS models are presented and deeply analyzed in terms of accuracy through several LESs with different spatial resolutions, i.e. grid spacings.

The first part of this thesis focuses on the basic theory of turbulence, the governing equations of fluid dynamics and their adaptation to LES. Furthermore, two important SGS models are presented: one is the Dynamic eddy-viscosity model (DEVM), developed by [Germano et al., 1991], while the other is the Explicit Algebraic SGS model (EASSM), by [Marstorp et al., 2009].

In addition, some details about the implementation of the EASSM in a Pseudo-Spectral Navier-Stokes code [Chevalier et al., 2007] are presented.

The performance of the two aforementioned models will be investigated in the following chapters, by means of LES of a channel flow, with friction Reynolds numbers $Re_\tau = 590$ up to $Re_\tau = 5200$, with relatively coarse resolutions. Data from each simulation will be compared to baseline DNS data.

Results have shown that, in contrast to the DEVM, the EASSM has promising potentials for flow predictions at high friction Reynolds numbers: the higher the friction Reynolds number is the better the EASSM will behave and the worse the performances of the DEVM will be.

The better performance of the EASSM is contributed to the ability to capture flow anisotropy at the small scales through a correct formulation for the SGS stresses.

Moreover, a considerable reduction in the required computational resources can be achieved using the EASSM compared to DEVM. Therefore, the EASSM combines accuracy and computational efficiency, implying that it has a clear potential for industrial CFD usage.

Abstract

Versione Italiana

Nelle Simulazioni a grandi vortici (*Large-eddy simulations, LES*), dei modelli per la scala di sottogriglia (*Sub-grid scale, SGS*) sono necessari per riprodurre l'influenza delle piú piccole scale della turbolenza, quindi non risolte, su quelle che invece vengono risolte direttamente.

Nel seguente lavoro sono presentati due modelli SGS, la cui accuratezza verrá poi analizzata attraverso varie LES a diverse risoluzioni spaziali, e quindi diversi intervalli di differenziazione.

La prima parte della tesi si concentra sulla teoria della turbolenza, partendo dalle equazioni costitutive della fluidodinamica, fino alla loro versione per LES.

Due importanti modelli SGS sono stati presentati: il primo é il modello *Dynamic eddy-viscosity model (DEVM)*, di [Germano et al., 1991], il secondo é il modello SGS Esplicito Algebrico, *Explicit Algebraic SGS model (EASSM)*, di [Marstorp et al., 2009].

Saranno inoltre forniti dettagli aggiuntivi sull'implementazione del modello EASSM su un codice di Fluidodinamica Computazionale (*Computational Fluid Dynamics, CFD*), Pseudo-Spettrale Navier-Stokes sviluppato nel Linné Flow Centre del Dipartimento di Ingegneria Meccanica del KTH di Stoccolma, da [Chevalier et al., 2007].

I seguenti capitoli verteranno sull'analisi della stima di un flusso in un canale, *channel flow*, fatta dai modelli descritti in precedenza, per un basso numero di Reynolds basato sull'attrito, $Re_\tau = 590$, fino a $Re_\tau = 5200$. I dati ottenuti da ciascuna simulazione verranno confrontati con dati di Simulazioni Numeriche Dirette (*Direct Numerical Simulations, DNS*).

Dai risultati ottenuti si puó concludere che, differentemente dal modello DEVM, l'EASSM ha promettenti potenzialitá nella stima del flusso ad alti numeri di Reynolds Re_τ: piú alto é tale numero, piú il modello EASSM dará risultati accurati, mentre le performances del DEVM peggioreranno.

Le migliori performance del modello Esplicito Algebrico possono senz'altro essere attribuite alla sua abilitá di calcolare in maniera corretta l'anisotropia alle piccole scale tramite una formulazione corretta degli stress di sottogriglia, SGS.

In conclusione, data la ridotta quantitá di risorse computazionali richiesta per effettuare simulazioni rispetto al DEVM, tale modello combina accuratezza e efficienza computazionale, tanto che puo' essere preso in considerazione per un utilizzo nella CFD industriale.

CONTENTS

TESI - VERSIONE ITALIANA

Prova ad immaginare un *pennacchio di fumo* fuoriuscente da una pipa di un uomo pensante, seduto su di una sedia a dondolo. Anche in questo piccolo aspetto della vita quotidiana la turbulenza gioca un ruolo fondamentale.

Il noto fisico Richard Feynman definii la *turbulenza* come il piú importante problema della fisica classica che ancora non é stato risolto.

Nel corso degli anni diversi scienziati hanno provato di comprendere il vero comportamento di tale fenomeno, la cui complessitá giace nelle equazioni che lo descrivono. Per un fluido Newtoniano, la turbolenza é definita dalle equazioni di Navier-Stokes, un sistema di equazioni non-lineari alle derivate parziali, la cui soluzione analitica ancora non é stata ottenuta.

Tuttavia, degli approcci alternativi per ottenere delle soluzioni sono stati sviluppati finora: un metodo consiste nell'effettuare degli esperimenti: tramite gallerie del vento siamo in grado di riprodurre flussi in svariate condizioni, dalle situazioni classiche di strato limite (moto su di una parete) e flusso in un canale, fino a casi piú complicati, come il flusso attorno ad un corpo tozzo (come una automobile) e un corpo aerodinamico, come un aeroplano.

Gli esperimenti hanno come fine principale l'analisi delle qualitá del flusso (come pressione e velocitá) attraverso delle sonde e delle tecniche di visualizzazione, come la Particle Image Velocimetry (PIV).

Un esempio molto recente di analisi sperimentale di turbolenza lungo un condotto a sezione circolare

(il cosiddetto *pipe*) ad alti numeri di Reynolds é senza dubbio il progetto CICLoPE, sviluppato da [Talamelli et al., 2009] nell'Universitá di Bologna.
D'altro canto, un approccio diverso é quello di sfruttare l'analisi numerica e passare alla implementazione del sistema N-S su codici di Fluidodinamica Computazionale.
Tuttavia, la soluzione numerica e completa fornita dalle Simulazioni Numeriche Dirette (DNS), in grado di descrivere la turbolenza *a qualsiasi scala*, non é sempre possibile a causa delle grandi risorse computazionali richieste, in particolare ad elevati numeri di Reynolds. Per questo motivo, l'obiettivo principale del progetto CICLoPE é quello di comprendere a pieno il fenomeno della turbolenza qualora non sia possibile ottenere dati tramite DNS.
Comunque, la tecnica DNS non é la sola in grado di riprodurre numericamente un preciso flusso. Una seconda possibilitá si chiama la *simulazione a grandi vortici* (Large-eddy simulation - LES); questa tecnica é in grado di raggiungere, con opportuni modelli per le piccole scale della turbolenza, una soddisfacente accuratezza computazionale con una ragionevole quantitá di risorse computazionali.
A tale avviso, la tesi verterá sull'impiego e il test di due modelli innovativi per le piccole scale della turbolenza; in particolare verrá messa a confronto l'accuratezza di ciascun modello con l'altro, rispetto anche i risultati forniti da DNS. Le simulazioni sono state compiute a tre diversi numeri di Reynolds; in particolare l'ultimo caso, di maggiore importanza, é relativo al massimo numero di Reynolds raggiunto finora da DNS.
La prima parte della tesi comprenderá la descrizione della turbolenza, sia da un punto di vista fisico che matematico. Saranno considerate le equazioni di N-S per un fluido Newtoniano, con flusso incomprimibile e turbolento, in un canale.
Nel secondo capitolo la tecnica LES sará espressa nei dettagli, mentre nel terzo verranno presentati due *modelli di scala sotto-griglia* (sub-grid scale - SGS). Il quarto capitolo spiegherá dei dettagli tecnici sull'implementazione delle simulazioni, dei due modelli, e della parallelizzazione MPI utilizzata. Nel quinto capitolo cenni di metodi statistici per l'analisi della turbolenza saranno affrontati. I risultati verranno presentati nel sesto capitolo, e infine saranno fornite delle conclusioni nel settimo capitolo.

INTRODUCTION

Imagine a smoking plume coming out from a pipe of a thinking man, this is a typical everyday life scenario where turbulence plays a main role. The physicist Richard Feynman defined it as *the most important unsolved problem of classical physics.*

Scientists along the years have tried to understand the real behaviour of this phenomenon, which gains its complexity because of the equations that describes it. For a Newtonian fluid, turbulence is traced by Navier-Stokes equations, a system of non-linear differential equations whose analytical solution has not been provided yet.

Anyway, alternative approaches has been developed across the years up to now: the most intuitive and old way to understand fluid motion is to make experiments: through the employment of wind tunnels we can reproduce the flow in several conditions, from the basical channel flow and boundary layer to the more complex ones, like the flow across a bluff body (like a car) or an airplane. This technique involves the analysis of the flow properties (like pressure and velocity) through probes and advanced visualization techniques such as Particle Image Velocimetry (PIV).

A recent example whose aim is to describe high Reynolds number turbulence across a pipe is nevertheless the CICLoPE experiment, a big project developed by

[Talamelli et al., 2009] in University of Bologna.

The second approach is thus to use numerical analysis in order to implement codes able to numerically solve Navier-Stokes system. However, the numerical and complete solution of the flow *at any*

scale is not always achievable because of the limited computational resources. For that reason, the main CICLoPE project's aim is to understand turbulence phenomena further the Reynolds number limit dictated by Direct Numerical Simulations.

However, DNS is not the only technique able to reproduce numerically a given flow. A possible second choice is called Large-eddy simulation; this technique is able to reach a satisfying computational accuracy with a reasonable amount of computational resources.

In this thesis Navier-Stokes equations for a Newtonian fluid and an incompressible flow in a turbulent channel flow scenario will be described in the first chapter, together with a physical description of turbulence. In the second chapter the Large-eddy simulation (LES) technique will be explained in detail, while in the third one two LES sub-grid scale models are shown. In chapter four some technical details of the implementation of the LES, of the models, with a particular focus on MPI parallelization are pointed out. Some theory about turbulence statistics will be faced in the fifth chapter. Results will be displayed in chapter six; conclusions are given in chapter seven.

CHAPTER

1

TURBULENCE

"Everybody is a genius. But if you judge a fish by its ability to climb a tree, it will live its whole life believing that it is stupid. (A.Einstein)"

1.1 Introduction to Turbulence

The phenomenon of turbulence is found in several applications, for example, combustion tumbling in Internal Combustion Engines (ICEs), the wake of a Formula 1 car, the jet spread by the nozzle of a supersonic aircraft engine.

In automotive engineering, for example, the study of aerodynamics around a car involves the characterization of a turbulent wall-bounded flow, called a *Boundary Layer*. It was intensively studied by L.Prandtl in 1904; here turbulence is the main responsible for friction and wake drag.

In a solid rocket motor nozzle, there's a generation of a plume, where turbulent motions of many scales can be observed; from eddies and bulges comparable in size to the width of the plume to the smallest scales the camera can resolve. Turbulence is of an unsteady, irregular, seemingly random

and chaotic nature, since the motion of every eddy is unpredictable.

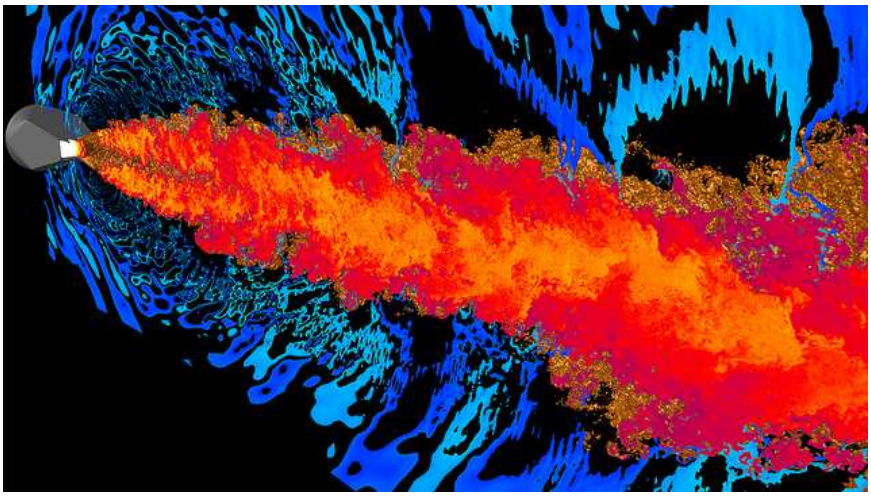

Figure 1.1 – Large-eddy simulation of jet from a rectangular nozzle. The rectangular nozzle is shown in gray with an isosurface of temperature (gold) cut along the center plane of the nozzle showing temperature contours (red/yellow). The acoustic field is visualized by (blue/cyan) contours of the pressure field taken along the same plane, from P.Moin.

While laminar flow is a smooth and steady flow motion, where any induced perturbations are damped out due to the relatively strong viscous forces, in turbulent flows other forces may be acting that counteract the action of viscosity. If such forces are large enough, the equilibrium of the flow is upset and the fluid cannot adapt suddenly to viscosity. The forces that upset this equilibrium can include buoyancy, inertia, or even rotation. In a channel, viscous and inertial forces acting on the fluid are proportional to

$$F_v \propto \nu L \tag{1.1}$$

$$F_i \propto V L^2 \tag{1.2}$$

where ν is the fluid viscosity, and L and V are the characteristic velocity and length scales. If the viscous forces on the fluid are large compared with others, any disturbances introduced in the flow will tend to be damped out. On the other hand, if the inertial forces become large, the fluid will tend to break up into eddies. For greater inertial forces, the eddies will break up into even smaller eddies. This will continue until we reach a small enough length scale (*eddy size*) on which the viscous forces dominate.

The largest of these eddies will be constrained by the physical size constraints on the flow (like channel diameter); the smaller eddies will be constrained by the viscous forces which act strongest at the smallest length scales. Therefore, one of the difficulties associated with the prediction of turbulent flow is that the range of length scales can be very large.

The description of turbulence involves different concepts like turbulence energy production, transfer and dissipation. Richardson's famous poem gives a good idea about turbulence:

Big whorls have little whorls
That feed on their velocity
And little whorls have lesser whorls
And so on to viscosity (in the molecular sense)

This is the description of the *energy cascade* concept. It states that turbulent flows can be considered as an agglomerate of eddies of different sizes. Large energy containing eddies are unstable and break down and transfer energy to smaller eddies. The process goes on till the smallest one, the Kolmogorov scale, where energy is dissipated into heat by viscous effects.
This is the great conclusion that Kolmogorov made in 1941, and his first hypothesis is completely based on that: at sufficiently high Reynolds number, the statistics of the small scales are universal and are determined solely by viscosity, ν, and the energy dissipation rate, ε.

Using dimensional analysis, it is possible to derive the Kolmogorov length scale η, timescale t_η and velocity scale v_η:

$$\eta = \left(\frac{\nu^3}{\varepsilon}\right)^{1/4}, \quad t_\eta = \left(\frac{\nu}{\varepsilon}\right)^{1/2}, \quad v_\eta = (\nu\varepsilon)^{1/4} \tag{1.3}$$

Then, in accordance to Richardson's poem, Kolmogorov made a second hypothesis, based on the fact that at sufficiently high Reynolds number the statistics of the scales which are sufficiently larger than η and much smaller than the largest energetic scales are solely described by ε. This hypothesis refers to the inertial range of scales. The kinetic energy spectrum of these scales can be described by

$$E(k) = C_k \varepsilon^{2/3} k^{-5/3} \tag{1.4}$$

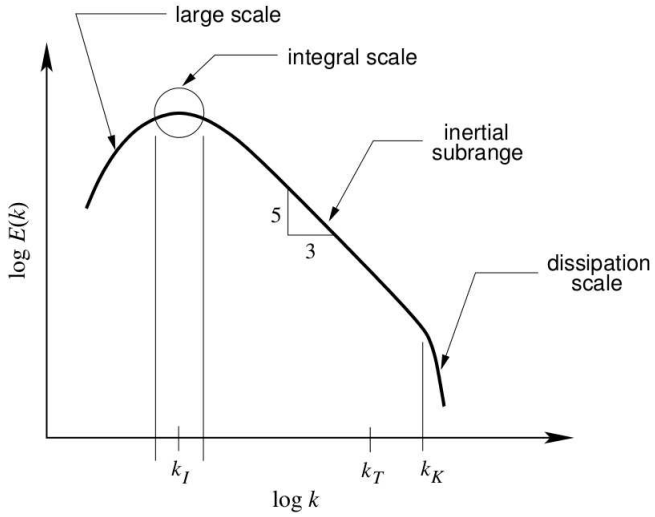

Figure 1.2 – Turbulence energy vs wavenumber spectrum, from J. M. McDonough.

where k is the wave number and $C_k \approx 1.5$ [Sreenivasan, 1995] is the Kolmogorov constant. From the last diagram, it's clear that turbulence has different behaviours according to the wavenumber. Basing on these concepts, we can distinguish four different regions:

1. the large scale, determined by the problem domain geometry;
2. the integral scale (Λ), which is an $\mathcal{O}(1)$ fraction (often taken to be ~ 0.2) of the large scale;
3. the Taylor microscale which is an intermediate scale, found in the Kolmogorov's inertial subrange ($\eta \ll \frac{2\pi}{\kappa} \ll \Lambda$)
4. the Kolmogorov (or *dissipation*) scale (η) which is the smallest of turbulence scales, the *inner scale*

1.1.1 3D Nature of Turbulence

Turbulence is rotational and a three-dimensional phenomenon. It is characterized by large fluctuations in vorticity, which are responsible for *vortex stretching* and *length scale reduction*. These characteristics are identically zero in two dimensions and these are the reasons why turbulence is hard to describe both analytically and numerically.
These three-dimensional dynamical mechanisms are highly complex and nonlinear, however the flow can be assumed as bi-dimensional for large scale 2D structures. These structures play a dominant role in the *transport* of scalar material. Nevertheless, three-dimensional motions are not negligible

in the smaller scale, where they are fundamental for mixing, most of all at molecular scales (e.g. in combustion problems).

1.1.2 Order & Randomness

Despite turbulence is chaotic, it consists of completely random motions that can aggregate in coherent structures. Typical examples are turbulent boundary layers and homogeneous turbulent shear flows, which exhibit horseshoe, or hairpin vortices (see figure 1.3) that appear to be inherent characteristics. Free shear flows like the mixing layer reveal coherent vortex structures very clearly, again even for very high turbulence intensities.

The concepts of order and randomness have also led to some new analytic approaches and new interpretations in the study of turbulence. The names of these disciplines are known as Chaos, Bifurcation Theory, and Dynamical Systems [McDonough, 2007]. These theories have been faced for the study of turbulence, in particular in the area of hydrodynamic stability and transition from laminar flow to turbulent one. Come to attention of mathematicians, physicists and engineers, these phenomena is of a remarkable non-linearity, which makes turbulence unpredictable and complex to describe.

As a nonlinear problem, it can be seen that the solutions to these problems with the same nonlinear equations with only slight differences in initial conditions, will rapidly diverge. Therefore, a suitable definition of turbulence must necessarily involve a complex dynamical system with many degrees of freedom.

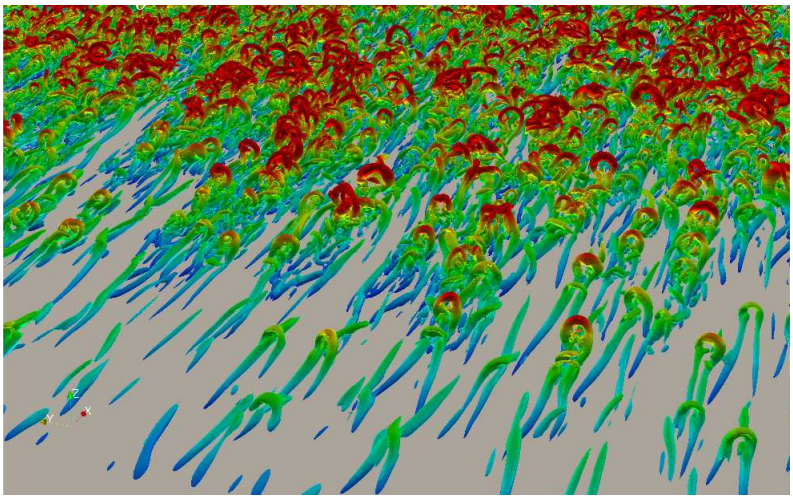

Figure 1.3 – Hairpin vortices on a turbulent boundary layer, from a DNS by P. Schlatter.

1.1.3 The Reynolds number

Turbulence can be seen also a play between inertial forces and viscous. Therefore the ratio between them is crucial in order to characterize a flow. The Reynolds number plays that role, and in turbulent flows holds

$$Re \stackrel{def}{=} \frac{UL}{\nu} \gg 1. \tag{1.5}$$

For many flows of practical importance (e.g. a flow on airplane wings) the Reynolds number can be on the order of $Re \sim 10^6$. This means that the viscous forces, that are molecular forces, act in smaller scales than in the large ones. However, in any turbulent flow the molecular viscosity is always important at some scale. As the flow Reynolds number increases, the region where viscous effects are remarkable, decreases in thickness and the velocity of the flow changes very rapidly from zero at the surface to the free-stream velocity at the outer edges of the boundary layer. Again, we see the tendency of the nonlinear inertial terms to generate discontinuities at high wavenumbers.
Once more, the Reynolds number can be interpreted also in terms of length and time scale ratios. Let's consider a duct of width L, with a flow velocity U. The time a fluid particle, with transverse velocity u' takes to cross the duct is called the *inertial time*, $T_i \sim L/u'$. At the same way, viscous forces have a time scale, $T_v \sim L^2/\nu$.
In a turbulent flow, the inertial time-scale will be mich less than the diffusive time-scale,

$$\frac{T_v}{T_{in}} = \frac{u'L}{\nu} > 1. \tag{1.6}$$

1.1.4 Navier-Stokes equations

Turbulence behaviour is completely described by the governing equations of fluid mechanics, i.e. the continuity and Navier-Stokes (N-S) equations. In case of incompressible flows, they are expressed in the following way on non-dimensional form:

$$\frac{\partial u_i}{\partial x_i} = 0; \quad \frac{\partial u_i}{\partial t} + \frac{\partial u_i u_j}{\partial x_j} = -\frac{\partial p}{\partial x_i} + \frac{1}{Re}\frac{\partial^2 u_i}{\partial x_j \partial x_j} \tag{1.7}$$

where Re is the characteristic Reynolds number of the flow, $u_i,\ i = 1, 2, 3$ are the velocity components, p is the pressure. Note that Einstein's summation convention is used here, where $i = 1, 2, 3$.

Together with the main flow field, sometimes we need also to understand phenomenas that involves the characterisation of a passive scalar.

By definition, the word passive refers to the condition that the resulting density differences are so small that the effect from the scalar on the flow is negligible. So a passive scalar can be heat or temperature in a flow or a concentration of a substance.
Therefore is also possible to use Navier-Stokes equations 1.7 to describe the development of a passive scalar, θ:

$$\frac{\partial \theta}{\partial t} + \frac{\partial u_i \theta}{\partial x_j} = \frac{1}{RePr} \frac{\partial^2 \theta}{\partial x_j \partial x_j} \tag{1.8}$$

where Pr is the Prandtl number, defined as the ratio of momentum diffusivity to thermal diffusivity:

$$Pr \overset{def}{=} \frac{\mu c_p}{k}.$$

1.2 Numerical approaches to N-S solution

There are several numerical approaches to solve the system 1.7. The most intuitive one is called *Direct Numerical Simulation, DNS*, whereby the governing euquations are solved without making any assumption, resolving all the scales from the smallest to the largest one. Therefore it provides all the information of a turbulent flow, without any approximations. Since the computational cost of DNS scales with the Reynolds number is $\sim Re^{37/14}$ [Choi and Moin, 2012], this is not affordable for practical engineering analyses at high Reynolds number.
So a more practical approach has been developed, based on the Reynolds' decomposition [Reynolds, 1894]:

$$u_i = \overline{u}_i + u_i', \quad \theta = \overline{\theta} + \theta' \tag{1.9}$$

where the overline represents the ensemble averaged quantity, and u_i' and θ' are the velocity and scalar components fluctuations, respectively.
Using the Reynolds decomposition in equations 1.7 and 1.8, and taking an ensemble average of all terms, the Reynolds-averaged N-S (RANS) equations are derived:

$$\frac{\partial \overline{u}_i}{\partial t} + \frac{\partial \overline{u}_i \overline{u}_j}{\partial x_j} = -\frac{\partial \overline{p}}{\partial x_i} + \frac{1}{Re}\frac{\partial^2 \overline{u}_i}{\partial x_j \partial x_j} - \frac{\partial \overline{u_i' u_j'}}{\partial x_j}, \quad \frac{\partial \overline{u}_i}{\partial x_i} = 0 \tag{1.10}$$

$$\frac{\partial \overline{\theta}}{\partial t} + \frac{\partial \overline{u}_i \overline{\theta}}{\partial x_j} = \frac{1}{RePr}\frac{\partial^2 \overline{\theta}}{\partial x_j \partial x_j} - \frac{\partial \overline{u_j' \theta'}}{\partial x_j} \tag{1.11}$$

Note that here turbulence is solely described by the Reynolds stress tensor $\overline{u_i' u_j'}$ and scalar flux vector $\overline{u_j' \theta}$. These terms have to be properly modelled in order to close the problem. Each model involves approximations which limits its accuracy. Therefore, this approach provides only an approximate simulation of the mean flow.
The first simple model was developed by Boussinesq in 1877. It is based on an *eddy viscosity* formulation

$$\overline{u_i' u_j'} - \frac{2}{3} K \delta_{ij} = -2\nu_T \overline{S}_{ij}, \quad \overline{S}_{ij} = \frac{1}{2}\left(\frac{\partial \overline{u}_i}{\partial x_j} + \frac{\partial \overline{u}_j}{\partial x_i}\right) \tag{1.12}$$

where $K = \overline{u_i' u_i'}/2$ is the mean turbulent kinetic energy, $\overline{S}_{ij}$ is the mean strain-rate tensor, the symmetric part of the mean velocity gradient tensor, ν_T is the eddy viscosity we use to model as the product of a certain scale with length Λ of the eddies and velocity V. Using dimensional analysis the eddy viscosity can be roughly estimated as

$$\nu_T \sim \Lambda V. \tag{1.13}$$

Eddy viscosity is then modeled accordingly to some characteristics of the flow.

For instance, **algebraic models** (or zero equation models) relate length Λ and velocity V to the mean velocity field and the flow geometry characteristics like velocity gradient, distance to the wall, thickness of the shear layer etc. These kind of models work quite well for the specific case that they are designed for, e.g. attached boundary layers and different types of thin shear layers. However, they don't give satisfactory results for general cases.

Better results can be achieved using **one-equation models**, they typically solve an additional transport equation for the turbulent kinetic energy, K, or the eddy viscosity, ν_T. One-equation models give good results for attached boundary layers and other thin shear layer flows, but for complex flows. A good example is the Spalart-Allmaras [Spalart and Allmaras, 1992] model (SA), that solves for the eddy viscosity. This is very suitable for aeronautical applications and actually is the standard model for external aerodynamics CFD analyses at Boeing.

Two-equations models solve two transport equations for two quantities that can be used for determining the length and velocity scale needed to compute the eddy viscosity. The most common are $K-\varepsilon$ and $K-\omega$ models, where transport equations for the turbulent kinetic energy, K and for the dissipation rate, ε or the turbulence frequency ω are solved. Nowadays the implementation of these models in commercial CFD codes (e.g., ANSYS Fluent) presents additional corrections that might be dependent on non-local quantities such as the wall distance. One important and most recent example is the Menter SST $K-\omega$ model [Menter, 1994], which is suitable for separated flows; it is the standard turbulence model used at Airbus.

Despite eddy viscosity two-equations models are still dominating in industrial CFD, there's a big demand for more accurate prediction of complex flow situations, including onset of separation, highly curved flows, rapidly rotating flows etc. In these situations, eddy viscosity Boussinesq' hypothesis (1.12) does not describe the real physics well. An effect of *decorrelation* caused by rotation occurs at high rotation rates, and generally the alteration of production to dissipation ratio is a direct consequence of that.

This phenomena, for instance, is an important aspect which eddy viscosity models does not take into account, because the model is insensitive to system rotation.

A better alternative to these models are the **Reynolds Stress Models**. They solve transport equations for each Reynolds stress components derived from the modelled N-S equations, in order to model the Reynolds stress tensor. This approach is more physically coherent, but it's compu-

tationally more expensive and complicated than the others. However, those differential Reynolds stress models can be simplified using the *weak equilibrium assumption* by Rodi [Rodi, 1992]. Details about this will be shown in 2. The algebraic relation is implicit in Reynolds stresses, but there are some explicit solutions ([Pope, 1975]; [Gatski and Speziale, 1993]; [Wallin and Johansson, 2000]). These models are called **Explicit Algebraic Reynolds Stress Models** (EARSM).

In particular, in the EA model [Wallin and Johansson, 2000] the flow anisotropy (a_{ij}) is described as an explicit expression in terms of the (normalized) mean strain and rotation tensors with additional scalar parameters. This leads to a *comparable computational efforts*, as compared to eddy viscosity two-equation models.

There's also an interesting analogy for the scalar θ modeling. Taylor developed an analogue way to formulate the eddy diffusivity model (EDM) for the mean turbulent scalar flux $\overline{u_i'\theta'}$ [Taylor, 1915]

$$\overline{u_i'\theta'} = -D_T \frac{\partial \overline{\theta}}{\partial x_i}, \quad D_T = \frac{\nu_T}{Pr_T} \tag{1.14}$$

where D_T is the eddy diffusivity coefficient and Pr_T the turbulent Prandtl number.

In an analogous way to $K-\varepsilon$ model, Nagano & Kim [Kim, 1988] developed the $K_\theta - \varepsilon_\theta$ model. The time scale $\tau_\theta = K_\theta/\varepsilon_\theta$, is used to compute $D_T \sim K\tau_\theta$.

Still, model 1.14 is not completely correct. According to Batchelor, eddy diffusivity assumes an alignment between the $\overline{u_i'\theta'}$ vector and the mean scalar gradient, so it has to be considered itself a tensor. The following expression will hold then:

$$\overline{u_i'\theta'} = -D_{ij} \frac{\partial \overline{\theta}}{\partial x_j} \tag{1.15}$$

Where the eddy diffusivity tensor can be rewritten as [Daly and Harlow, 1970]

$$D_{ij} = -C_\theta \tau_\theta \overline{u_i'u_j'} \frac{\partial \overline{\theta}}{\partial x_j} \tag{1.16}$$

and C_θ is a model coefficient.

In the same way, scalar can be modelled with an Explicit Algebraic model, in this case called the Explicit Algebraic Scalar Flux Models (EASFM).

A trade-off between accuracy and computational effort is Large-eddy simulations (LES) of turbulent flows. In LES there's a separation of scales, in the sense that only large-scale eddies are resolved, while the remaining small scales (which are called sub-grid scales, SGS) are modelled, once the resolved scales have been computed. The separation of scales is generally done using a grid. Together with filtering, LES focuses its turbulence prediction accuracy on a *time-dependent solution*

of the Navier-Stokes equations. This is therefore a physically-coherent approach since turbulence is unstationary.

Despite more computationally expensive than RANS, LES gives a better description of turbulence, and unlike DNS, is able to provide a good resolution of the flow in an acceptable amount of computational time. Recently, that time has been estimated by Choi & Moin [Choi and Moin, 2012], to scale as $\sim Re^{26/14}$.

A fair and simplified distinction between DNS and LES can be noticed having a look to the vortical structures, for both of the cases, in figure 1.4. At a first glance, we can see that in LES vortical structures are underestimated and fewer, compared to the DNS, which is able, instead, to give a complete and detailed description of them.

The first LES model was developed by Smagorinsky [Smagorinsky, 1963] for meteorological applications using an eddy viscosity assumption in the SGS model. This model has been improved later on by Germano [Germano et al., 1991] introducing the *dynamic procedure*, which gives a correct asymptotic near-wall behaviour of the eddy viscosity, and improved transitional flows predictions. However, eddy-viscosity models are not anisotropic, that is, they are not able to capture flow anisotropy well, a feature of the flow, which is not neglectable near the walls.

For that reason several non-linear models (which are of course anisotropic), have been developed recently, and some of them will be described in detail in chapter 3. In particular, the aim of this thesis is to test the accuracy in flow prediction of the Explicit Algebraic SGS model (EASSM), developed by Marstorp [Marstorp et al., 2009].

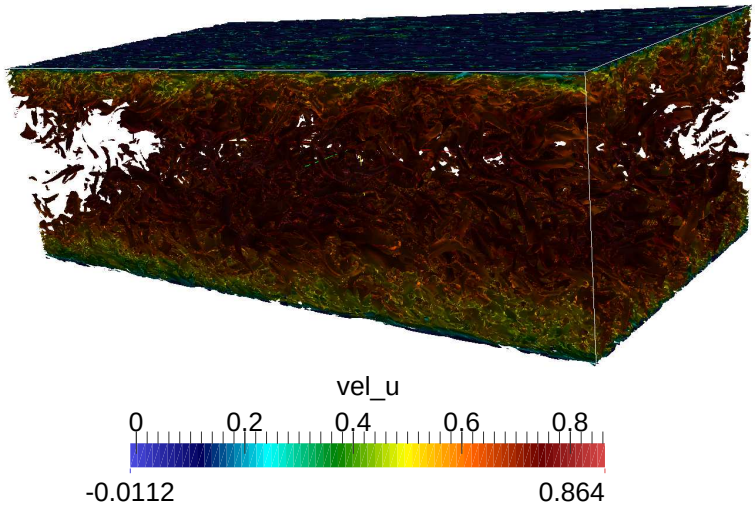

a)

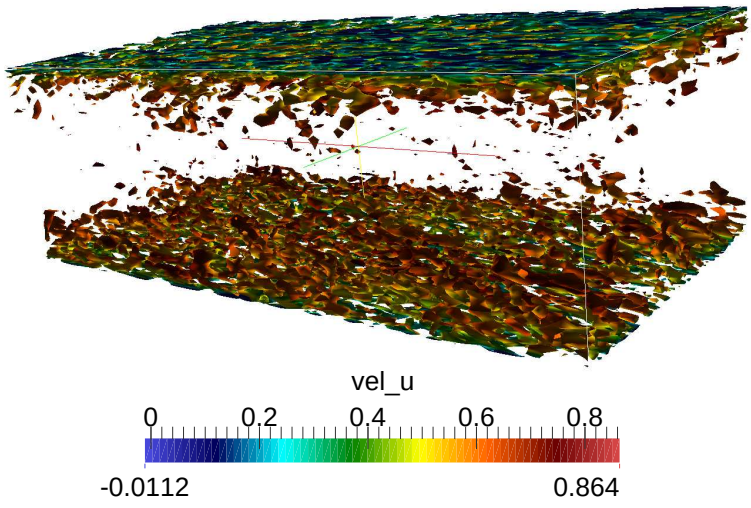

b)

Figure 1.4 – Vortical structures in turbulent channel flow at $Re_\tau = 590$, visualized by isosurfaces of λ_2, colored by the velocity magnitude, from a) DNS by P.Schlatter b) LES simulation with the Explicit Algebraic model .

1.3 A particular case: Turbulent Channel Flow

Mathematical models for fluid dynamics have been already defined. In order to solve the models, a mathematical problem needs to be defined in a proper time and space domains.
According to the space domain, in a different geometry, physical quantities and the flow will behave in a different way. For this reason we need to set a particular case, so that the flow can be univocally classified.
In this thesis we are considering the case of Channel Flow, with the following properties:

- **turbulent**, in the sense that the Reynolds number is sufficiently high such that the regime can be assumed as turbulent;
- **fully developed**, so that velocity statistics are constant along x-axis. In other words, the flow is *statistically stationary* and *statistically one-dimensional* [Pope, 2000], with velocity statistics only variable along the y-axis. In other words:

$$\langle u \rangle = U = U(y), \quad \langle v \rangle = V = 0, \quad \overline{u'v'} = \overline{u'v'}(y) \tag{1.17}$$

Channel flow belongs to the *wall-bounded shear flows* class: flow motion is contained between two solid surfaces. Therefore, *no-slip conditions* are imposed on the walls, where the fluid velocity is assumed to be zero. The following picture shows the qualitative behaviour of the velocity.

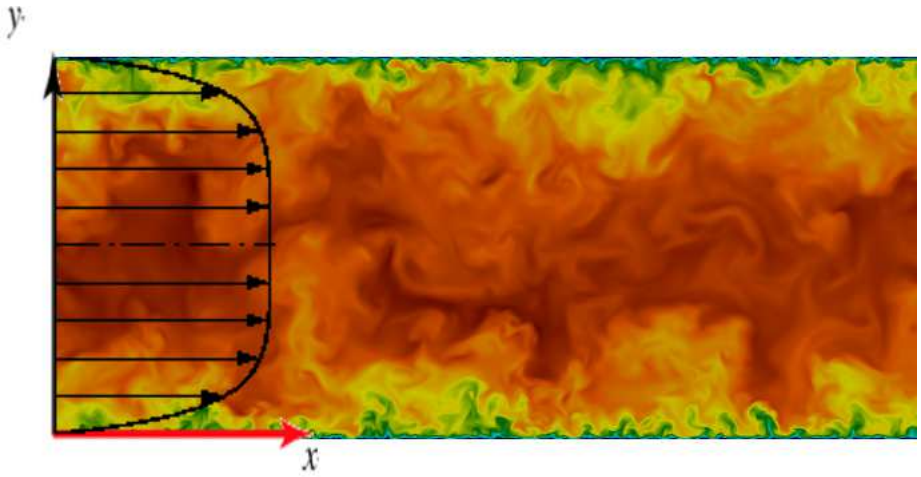

Figure 1.5 – Channel Flow mean velocity profile, with u' fluctuations contour plot in the background, from Lee & Moser DNSs at $Re_\tau = 1000$ [Lee and Moser, 2014]

Furthermore, a statistically symmetric flow geometry w.r.t. the mid-plane $y = \delta$ is confirmed by experiments; therefore the statistics of (u, v, w) at y are the same as those of $(u, -v, w)$ at $2\delta - y$.

Reynolds number is always used to characterize the flow, in this case we will refer to two particular Reynolds numbers,

$$Re_\tau \stackrel{def}{=} \frac{u_\tau \delta}{\nu} \tag{1.18}$$

$$Re_b \stackrel{def}{=} \frac{\overline{u}\delta}{\nu} \tag{1.19}$$

where 1.18 is based on the friction velocity u_τ, defined as follows:

$$u_\tau \stackrel{def}{=} \sqrt{\tau_W/\rho} \tag{1.20}$$

τ_W is the mean wall shear stress and δ is the channel half-width.
The bulk velocity $\overline{u}$ in 1.19, is defined as

$$\overline{u} = \frac{1}{2\delta}\int_0^{2\delta} \langle u \rangle dy \tag{1.21}$$

For a turbulent channel flow, the following result holds:

$$Re_\tau \approx 0.166 Re_b^{0.88} \tag{1.22}$$

Note that the specified formula 1.22 will be used for the derivation of Re_b, which will be considered as an input quantity in the computations.
As previously stated, channel flow is a wall-bounded shear flow. In a boundary layer or a wall-bounded shear flow the characteristic length for streamwise development is much larger than the cross-stream extent of the region with significant velocity variation.
So its behaviour can be observed studying a two-dimensional steady flow scenario with the *thin shear layer approximation* [Johansson and Wallin, 2012]. This approximation states that the characteristic streamwise development length, L is much larger than δ, the shear layer thickness. As we will confirm later, in channel flow there will be a layer, whose thickness is small compared to the characteristic length, whereby viscous effects friction depends on.
Thanks to this approximation, the Navier-Stokes equations can be simplified to the *thin shear layer equation*:

$$U\frac{\partial U}{\partial x} + V\frac{\partial U}{\partial y} = -\frac{1}{\rho}\frac{dP_0}{dx} + \frac{\partial}{\partial y}\underbrace{\left(\nu\frac{\partial U}{\partial y} - \overline{u'v'}\right)}_{total\ shear\ stress} \tag{1.23}$$

where P_0 if the pressure at the wall. Note that all the velocities in 1.23 are mean values, and the only component responsible for turbulence is the last one on the right-hand-side, which is called the *Reynolds stress*. Together with the viscous stress, the Reynolds stress generates the total shear stress.

In particular, using the channel flow assumptions given in 1.17, the thin-shear layer equation becomes

$$0 = -\frac{1}{\rho}\frac{dP_0}{dx} + \frac{d}{dy}\left(\nu\frac{dU}{dy} - \overline{u'v'}\right) \tag{1.24}$$

Integrated in the wall-normal direction it reads

$$0 = -\frac{1}{\rho}\frac{dP_0}{dx}y + \nu\frac{dU}{dy} - \underbrace{\nu\frac{dU}{dy}\bigg|_{y=0}}_{u_\tau^2} - \overline{u'v'} + 0 \tag{1.25}$$

At the centerline ($y = \delta$) the total shear stress is zero, therefore we have the following condition:

$$\frac{1}{\rho}\frac{dP_0}{dx} = -\frac{u_\tau^2}{h} \tag{1.26}$$

meaning that the pressure gradient is related to the friction velocity and the width of the channel. Plugging this relation in 1.25, we can see that the total shear stress develops linearly across the channel:

$$\nu\frac{dU}{dy} - \overline{u'v'} = u_\tau^2\left(1 - \frac{y}{\delta}\right) \tag{1.27}$$

which in wall units becomes

$$\frac{dU^+}{dy^+} - \overline{u'v'}^+ = \left(1 - \frac{y^+}{\delta^+}\right) \tag{1.28}$$

where the quantities y^+ and δ^+ are scaled by the inner (viscous) lengthscale

$$y^+ \overset{def}{=} \frac{y}{l_*} = \frac{yu_\tau}{\nu}$$

Considerations. Depending on the region considered, equation 1.28 assumes different forms. In the outer layer, where viscous effects are negligible, the left-hand-side of 1.28 becomes

$$-\overline{u'v'}^{+} = 1 - \frac{y^+}{\delta^+} \tag{1.29}$$

On the other hand, close to the wall, $y/\delta << 1$, viscous effects will be not negligible anymore, therefore the following relation holds

$$\frac{dU^+}{dy^+} - \overline{u'v'}^{+} \approx 1 \tag{1.30}$$

that is compatible with the law of the wall, since there's not influence of the Reynolds number. It's a *constant stress* region:

$$U^+ \stackrel{def}{=} \frac{U}{u_\tau} = \Phi_1(y^+) \tag{1.31}$$

$$\overline{u'v'}^{+} = \Phi_2(y^+) \tag{1.32}$$

Moreover, for large Reynolds numbers, we can also assume that there is an *overlap region* for wall distances y,

$$\ell_* << y << \delta$$

where δ is boundary layer thickness and ℓ_* the viscous lengthscale. This is a particular region where outer and inner layer descriptions hold simultaneously.
Derivating the following 1.31 w.r.t. y^+ we'll have an expression which is independent of lengthscale. Therefore holds

$$y^+ \frac{d\Phi_1(y^+)}{dy^+} \equiv const \tag{1.33}$$

so that, once integrated, it gives a *logarithmic law*:

$$\Phi(y^+) = \frac{1}{\kappa} lny^+ + B \tag{1.34}$$

where $\kappa = 0.38$ is the Kármán constant and B=4.1, according to observations. In the following figure 6.22 a mean velocity diagram is shown, together with the *law of the wall* and the *log law*, at $Re_\tau = 5200$.

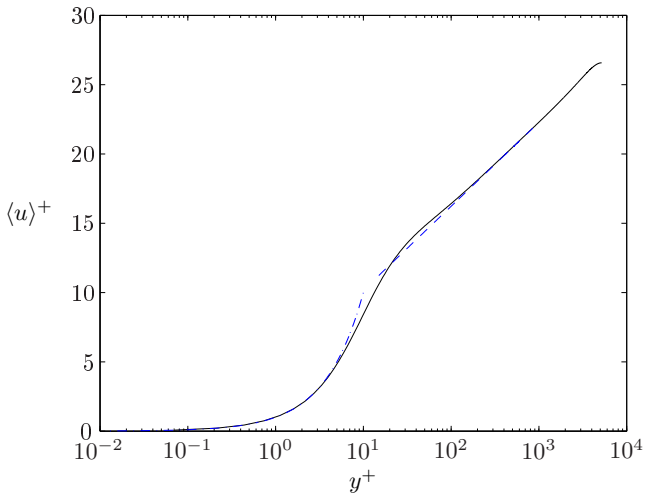

Figure 1.6 – – : $< u >^+$ vs y^+, at $Re_\tau = 5200$, from [Lee and Moser, 2014], –.– : law of the wall, – – : log law

As we can see from the previous picture, the first velocity region called *viscous sublayer*, follows the law of the wall, and it extends out to approximately $y^+ = 5$. Despite the absolute magnitude of the turbulent fluctuations are small in this region, the relative (wall-parallel) intensities are large. As we increase y^+, we will have a *buffer region*, where the maximum turbulence production is at $y^+ = 12$ and the maximum turbulence intensity at $y^+ = 15$. *Log-layer* starts between $50 < y^+ < 200$, and it extends to $y/\delta \approx 0.15$, where δ is the channel half-width. Beyond the log layer, there's finally the *outer region*.

The maximum turbulence production and Reynolds stress.

The turbulence production in the near-wall region of wall-bounded flows can be formulated as

$$\mathcal{P}^+ = -\frac{\overline{u'v'}}{u_\tau^2}\frac{dU^+}{dy^+} \simeq \left(1 - \frac{dU^+}{dy^+}\right)\frac{dU^+}{dy^+} \tag{1.35}$$

The latter approximation is valid if viscous effects are small. From this we can derive that the maximum production is found where

$$\frac{dU^+}{dy^+} = \frac{1}{2} \tag{1.36}$$

which leads to

$$\mathcal{P}^+_{max} = \frac{1}{4} \tag{1.37}$$

Therefore the turbulent production is maximum whereas both viscous and Reynolds stresses are exactly the same, that is in the near-wall region; it generally happens when $y^+ \approx 12$. Moreover, it's

also possible to estimate where the maximum Reynolds shear stress occurs. Deriving equation 1.28 w.r.t. y^+, and denoting the Reynolds shear stress as τ, normalized by inner units, the following relation holds:

$$\frac{d^2U^+}{dy^{+^2}} + \frac{d\tau^+}{dy^+} = -\frac{1}{\delta^+} \tag{1.38}$$

if we also assume that the Reynolds stress is maximum in the log-region, taking the derivative 1.34 w.r.t y^+ we have

$$\frac{d^2U^+}{dy^{+^2}} = -\frac{1}{\kappa y^{+^2}} \tag{1.39}$$

meaning that the maximum of the Reynolds stress is at

$$y^+_{max} = \sqrt{\frac{h^+}{\kappa}} = \sqrt{\frac{Re_\tau}{\kappa}} \tag{1.40}$$

Then, in terms of outer scale we can say that the position where the Reynolds stress reaches its maximum is proportional to $Re_\tau^{-1/2}$:

$$\frac{y_{max}}{h} = \kappa^{-1/2} Re_\tau^{-1/2} \propto Re_\tau^{-1/2} \tag{1.41}$$

This also can be proved using DNS results at different friction Reynolds numbers. An example of Reynolds stress profiles is shown in figure 1.7.

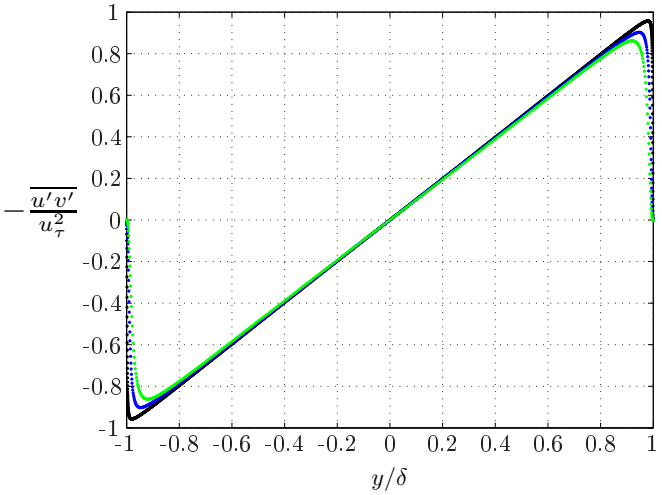

Figure 1.7 – $-\overline{u'v'}$ normalized by u_τ vs y/δ, from [Lee and Moser, 2014], $\cdots$: $Re_\tau = 550$, $\cdots$: $Re_\tau = 1000$, $\cdots$: $Re_\tau = 5200$

The maximum Reynolds shear stress can be derived as well, using the relation 1.38 and 1.40, together with the log-law:

$$\tau^+_{max} = 1 - \frac{y^+_{max}}{h^+} - \frac{1}{\kappa y^+_{max}} = 1 - \frac{2}{\sqrt{\kappa h^+}} = 1 - \frac{2}{\sqrt{\kappa Re_\tau}}. \tag{1.42}$$

We already have talked about turbulence and its production in a qualitative sense, but, in order to describe it properly and to understand the phenomenon in a complete and detailed sense, a focus on the three components of the velocity, they are u', v' and w', is necessary. As we'll see in the next chapters, the computations of these components play an important role in the validation of a LES model.

In particular, it's possible to derive the Reynolds stress tensor making the square of the root-mean-square value of these three components:

$$\overline{u'_i u'_j} = \begin{pmatrix} \overline{u'u'} & \overline{u'v'} & \overline{u'w'} \\ \overline{u'v'} & \overline{v'v'} & \overline{v'w'} \\ \overline{u'w'} & \overline{v'w'} & \overline{w'w'} \end{pmatrix}. \tag{1.43}$$

In the following picture all the components of the Reynolds stress are shown. Important to underline is the relation between the maximum turbulence production, and the peaks in the Reynolds stress profiles.

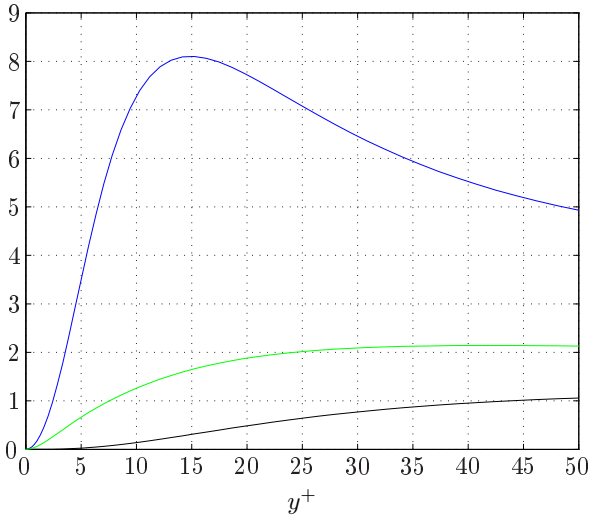

Figure 1.8 – Variances of the velocity fluctuations, normalized in wall units, from DNS of [Lee and Moser, 2014] at $Re_\tau = 1000$, —: $\overline{u'u'}^+$, — : $\overline{v'v'}^+$, —: $\overline{w'w'}^+$

,

Anisotropy of the flow. A fundamental aspect, which is strongly relevant for the complete understanding of the aforementioned work, is the concept of anisotropy in turbulence.
From a physical point of view, anisotropy is a property of the flow which is not aligned with the velocity direction and the velocity gradient.
For a fully-developed channel flow the quantities $\overline{u'w'}$ and $\overline{v'w'} = 0$ are zero. The Reynolds stress tensor becomes:

$$\tau_{ij} = -\rho \begin{pmatrix} \tau_{11} & \overline{u'v'} & 0 \\ \overline{u'v'} & \tau_{22} & 0 \\ 0 & 0 & \tau_{33} \end{pmatrix}. \tag{1.44}$$

in case of isotropic turbulence, the diagonal terms are equal, i.e. $\tau_{11} = \tau_{22} = \tau_{33}$ and all the deviatoric terms are zero. Therefore, for a specific LES model, the ability to capture the anisotropy of the flow consists in reproducing different diagonal terms, i.e. $\overline{u'u'} \neq \overline{v'v'} \neq \overline{w'w'}$.

CHAPTER

2

LARGE EDDY SIMULATION

"Anxiety is the hand maiden of creativity. (T.S. Eliot)"

Reynolds-averaged Navier Stokes (RANS) equations-based simulations are able to solve only the mean velocity field of the flow. RANS simulations rely heavily on modelling since all turbulent motions are modelled and therefore they are not always accurate.
In Direct Numerical Simulations (DNS), the unsteady Navier-Stokes equations are solved without using models. Therefore, DNS is very accurate. However, the computational power demand for DNS is too large for industrial applications. Therefore, a new method which combines a reasonable flow prediction accuracy with a limited amount of computational cost has been strongly required in recent years.
Large-eddy simulation (LES) represents an alternative that fits those requirements. This particular method employs a *separation of scales* [Rasam, 2014]: a filtering operation decomposes the velocity field (generally together with a scalar one) into a resolved part, represented by the computational grid, and an unresolved part, which is modelled through physically realistic models. In other words, LES could be considered a 2-step method:

1. the solution of the large scales of turbulence on a relatively coarse grid ;

2. the modelling of the smaller unresolved scales, the so-called *subgrid-scales (SGS)*, based on the resolved velocity field.

2.1 The filtering operation

Step 1. Let's consider now a general time and space-dependent function $\phi(x,t)$. The filtering operation consists of a convolution of a kernel G_Δ on that function (Leonard, 1975), over the domain D of the grid:

$$\widetilde{\phi}(x,t) = \int_D \phi(x,t) G_\Delta(x-\xi) d\xi \tag{2.1}$$

There are several options for the filter: the commonly used ones are spectral cutoff, box and Gaussian filters. In spectral codes, spectral filters are the most suitable ones for filtering, since they act on a spectral space (where the code works on) and are more precise. Figure below shows the difference between the different kinds of filtering methods.

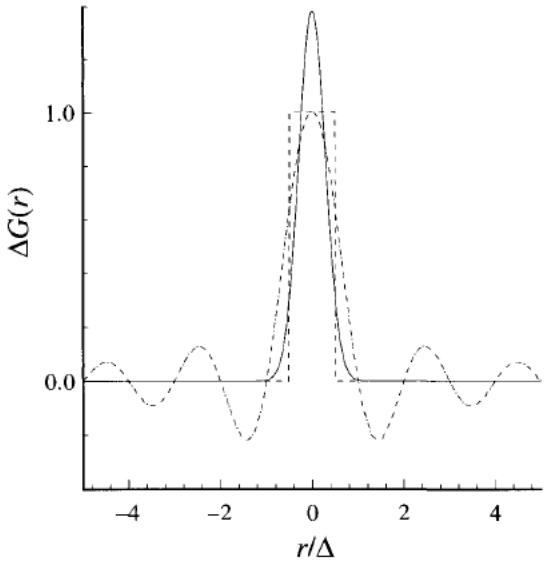

Figure 2.1 – –.– : Sharp-spectral filter, —- : Gaussian filter, – – : Box filter, $r = \xi$, from [Pope, 2000]

Remark. If $\phi(x,t) = \phi(x)$ the operator G_Δ is homogeneous. Moreover, the filtered velocity

field $\widetilde{u}(x,t)$ is not a deterministic variable, implying that

$$\widetilde{\widetilde{u}}(x,t) \neq \widetilde{u}(x,t), \quad \widetilde{u'}(x,t) \neq 0.$$

2.2 Governing equations of LES and the closure problem

The filtering operation leads to the filtered Navier-Stokes equations:

$$\frac{\partial \widetilde{u}_i}{\partial x_i} = 0; \quad \frac{\partial \widetilde{u}_i}{\partial t} + \frac{\partial \widetilde{u}_i \widetilde{u}_j}{\partial x_j} = -\frac{\partial \widetilde{p}}{\partial x_i} + \frac{1}{Re}\frac{\partial^2 \widetilde{u}_i}{\partial x_j \partial x_j} - \frac{\partial \tau_{ij}^{SGS}}{\partial x_j} \tag{2.2}$$

here τ_{ij} is the SGS stress tensor. Leonard [Leonard, 1974] proposed a possible decomposition of non-linear terms (i.e. the SGS stress tensor), in the following way:

$$\tau_{ij}^{SGS} = \widetilde{u_i u_j} - \widetilde{u}_i \widetilde{u}_j = L_{ij} + C_{ij} + R_{ij} \tag{2.3}$$

where

$$L_{ij} = \widetilde{\widetilde{u}_i \widetilde{u}_j} - \widetilde{u}_i \widetilde{u}_j, \tag{2.4}$$

$$C_{ij} = \widetilde{\widetilde{u}_i u'_j} - \widetilde{\widetilde{u}_j u'_i} \tag{2.5}$$

$$R_{ij} = \widetilde{u'_i u'_j}, \tag{2.6}$$

and $u'_i = u_i - \widetilde{u}_i$.

In the Leonard decomposition R_{ij} is the Reynolds subgrid tensor and represents the interaction between subgrid-scales; C_{ij} is the cross-stress tensor and accounts for large vs small scale interactions; finally L_{ij}, the Leonard tensor, gives the interactions between the large scales.
τ_{ij}^{SGS} is the unknown additive part in the filtered Navier-Stokes equation, and therefore needs to be modelled.

2.3 An example of a closure: the Eddy Viscosity Model (EVM)

Step 2. There are several ways to model the subgrid scale stress tensor. As previously written, the first and simple model was developed by Smagorinsky [Smagorinsky, 1963], for meteorological applications. It originates from the RANS model, taking into account Boussinesq's hypothesis. The EVM consists of a linear formulation of the deviatoric part of τ_{ij}^{SGS},

$$\tau_{ij}^{SGS} = \underbrace{\frac{\tau_{kk}}{3}\delta_{ij}}_{isotropic} - 2 \underbrace{\nu_{SGS}}_{\substack{EVM \\ contribution}} \widetilde{S}_{ij} \tag{2.7}$$

where

$$\nu_{SGS} = (C_s\widetilde{\Delta})^2|\widetilde{S}| \tag{2.8}$$

$\widetilde{S}_{ij}$ and $|\widetilde{S}|$ are the resolved strain-rate tensor and its magnitude, respectively. $\widetilde{\Delta}$ is the filter scale, ν_{SGS} is the SGS eddy viscosity, and C_s is the model coefficient, the Smagorinsky coefficient.

Note that ν_{SGS} is a constant rather than dependent of direction. According to the recent paper of Spalart [Spalart, 2015], in a simple shear flow with two of the axes aligned with the velocity direction and the gradient direction, such that the strain tensor S_{ij} have zero and equal diagonal terms, this model predicts constant and equal diagonal terms of the Reynolds stress tensor, i.e. $\tau_{11} = \tau_{22} = \tau_{33}$.

Therefore EVM can be considered an *isotropic* model, since ν_{SGS} doesn't take into account any effect of anisotropy.
As we'll discuss further, this model can be improved using a dynamic procedure, where the C_s coefficient is computed during the simulation.

2.4 Subgrid-scale dissipation

An important aspect of LES is the impact of SGS on the resolved scales. In other words, LES predictions are strongly dependent on the contribution of τ_{ij}^{SGS} tensor on the resolved kinetic energy $K = \widetilde{u}_i\widetilde{u}_j/2$. Consider the kinetic energy equation

$$\underbrace{\frac{\partial K}{\partial t} + \frac{\partial}{\partial x_j}(\widetilde{u}_j K)}_{advection} = \underbrace{-\nu\frac{\partial \widetilde{u}_i}{\partial x_j}\frac{\partial \widetilde{u}_i}{\partial x_j}}_{\substack{viscous \\ dissipation}} \underbrace{- \frac{\partial}{\partial x_i}\left(\widetilde{u}_i\widetilde{p} + \nu\frac{\partial K}{\partial x_i} - \widetilde{u}_i\tau_{ij}\right)}_{diffusion} + \underbrace{\tau_{ij}^{SGS}\widetilde{S}_{ij}}_{\substack{-SGS \\ dissipation}} \tag{2.9}$$

Since LES by definition, are carried out for large scales, and the grid scale is much larger than Kolmogorov one, the viscous dissipation term is so small so that it is negligible compared to the others. From a physical point of view, *diffusion term transfers energy in space, but not in a volume-averaged sense* [Rasam, 2014]. For that reason, an additional term is therefore required in order to reproduce the correct energy transfer from the large to the smaller scales. SGS dissipation covers that role

$$\Pi = -\tau_{ij}^{SGS}\widetilde{S}_{ij} \tag{2.10}$$

The mean SGS dissipation behaves as a sink term, while the instantaneous one gives negative (backscatter) and positive (forward scatter) contributions in the transfer.
The following picture shows the SGS dissipation (red line), together with the dissipation of the resolved scales (blue line); their total contribution is shown by the red line.

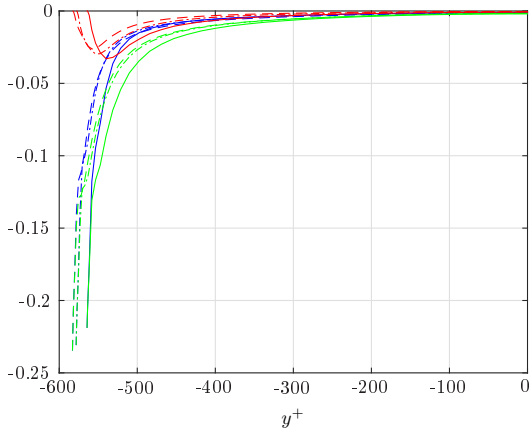

Figure 2.2 – Dissipation of the resolved scales, ε, together with the SGS dissipation, Π, and their sum – at increasing resolutions, from LES at $Re_\tau = 590$ shown in chapter 6.

The previous consideration leads to the fact that an investigation on SGS dissipation behaviour is very important in an accuracy assessment of LES.
Based on this principle, several investigations have been carried out by Chow & Moin [Chow and Moin, 2003], Ghosal [Ghosal, 1996] and Kravchenko & Moin [Kravchenko et al., 1996].
Geurts & Fröhlich [Geurts and Fröhlich, 2002] introduced the SGS activity parameter, defined as follows

$$s = \frac{<\varepsilon^{SGS}>}{<\varepsilon^{SGS}> + <\varepsilon^{\mu}>} \tag{2.11}$$

where $<\varepsilon^{\mu}> = 2\mu\widetilde{S}_{ij}\widetilde{S}_{ij}$ is the viscous dissipation.
With increasing resolution, SGS dissipation decreases while viscous one increases, therefore s becomes smaller. A remarkable aspect is that, the coarser is the resolution , the bigger is s . This can be proved having a look at 2.11: if we use a coarse grid, the resolution will be smaller such that viscous dissipation will be negligible, and s will reach its maximum unity value. This occurs when the cutoff filter of the LES is well in the inertial subrange and the viscous dissipation is rather

small.

Starting from the previous definition, Geurts & Fröhlich [Geurts and Fröhlich, 2002] defined an error norm as

$$\delta_E = \left| \frac{E_{LES} - \widetilde{E}_{DNS}}{\widetilde{E}_{DNS}} \right| \tag{2.12}$$

where E_{LES} is the mean resolved kinetic energy integrated over the flow domain, while $\widetilde{E}_{DNS}$ is the same quantity, computed from filtered DNS data instead, with the same filter width as in the LES.

The accuracy assessment consists of computing the relation between δ_E and s: in the picture below [Rasam et al., 2011] it is shown that the relative error δ_E drops almost exponentially with decreasing s (i.e. high resolution); results refer to a LES with the explicit algebraic SGS stress model (EASSM) [Marstorp et al., 2009] at $Re_\tau = 934$, for six different resolutions. This result shows that with increasing resolution the SGS contribution becomes smaller and the accuracy of the LES higher. In other words, *the resolution of the LES must be sufficiently high to obtain an acceptable solution.*

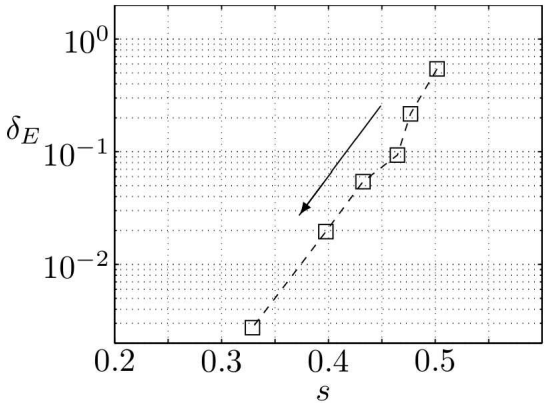

Figure 2.3 – Normalized error δ_E of the resolved kinetic energy, integrated over the channel width [Rasam et al., 2011] w.r.t. the filtered DNS value vs s. Arrow points to increasing resolution cases.

CHAPTER

3

SUBGRID-SCALE STRESS MODELS FOR LES

"Logic will get you from A to B.
Imagination will take you everywhere. (A.Einstein)"

In this chapter two different LES models are going to be analyzed; the first one is an improvement of the classic Smagorinsky model, the Dynamic EVM.
The second one is a particular non-linear model using an explicit algebraic formulation for the SGS stress tensor.
In the following section a decomposition of the SGS stress tensor is given.

3.1 Tensorial polynomial formulation of the SGS stress tensor

A useful approach that leads to several non-linear models is based on a decomposition of the SGS stress tensor, through a polynomial expansion.

Similar to RANS approach for Reynolds stress closures, SGS stress tensor can be expressed in terms of strain and rotation rate tensors.

Lund & Novikov [Lund and Novikov, 1993] expressed the deviatoric part of the SGS stress tensor $\tau_{ij}^{SGS,d}$ as a general tensorial function of the filtered strain-rate $\widetilde{S}_{ij}$ and rotation-rate $\widetilde{\Omega}_{ij}$ tensors, the Kronecker delta δ_{ij} and the filter size $\widetilde{\Delta}$ as

$$\tau_{ij}^{SGS,d} = \tau_{ij}^{SGS} - \frac{1}{3}\tau_{kk}\delta_{ij} = f(\widetilde{S}_{ij}, \widetilde{\Omega}_{ij}, \delta_{ij}, \widetilde{\Delta}) \tag{3.1}$$

where

$$\widetilde{S}_{ij} = \frac{1}{2}\left(\frac{\partial \widetilde{u}_i}{\partial x_j} + \frac{\partial \widetilde{u}_j}{\partial x_i}\right), \quad \widetilde{\Omega}_{ij} = \frac{1}{2}\left(\frac{\partial \widetilde{u}_i}{\partial x_j} - \frac{\partial \widetilde{u}_j}{\partial x_i}\right). \tag{3.2}$$

As Pope [Pope, 1975] showed the Reynolds stresses in RANS, τ_{ij} can be formulated as a tensor polynomial with ten elements of differents powers of $\widetilde{S}_{ij}$ and $\widetilde{\Omega}_{ij}$ and their combination.

Coefficients are functions of $\widetilde{S}_{ij}$ and $\widetilde{\Omega}_{ij}$ invariants or both, and they are derived using the Cayley-Hamilton theorem:

$$\boldsymbol{\tau}^d = \sum_{k=1}^{10} \beta_k \mathbf{T}^{(k)}, \tag{3.3}$$

so that the ten polynomial tensors are:

$\mathbf{T}^{(1)} = \widetilde{\mathbf{S}}$

$\mathbf{T}^{(2)} = \widetilde{\mathbf{S}}^2 - \frac{1}{3} II_S \mathbf{I}$

$\mathbf{T}^{(3)} = \widetilde{\mathbf{\Omega}}^2 - \frac{1}{3} II_\Omega \mathbf{I},$

$\mathbf{T}^{(4)} = \widetilde{\mathbf{S}}\widetilde{\mathbf{\Omega}} - \widetilde{\mathbf{\Omega}}\widetilde{\mathbf{S}}$

$\mathbf{T}^{(5)} = \widetilde{\mathbf{S}}^2\widetilde{\mathbf{\Omega}} - \widetilde{\mathbf{\Omega}}\widetilde{\mathbf{S}}^2$

$\mathbf{T}^{(6)} = \widetilde{\mathbf{S}}\widetilde{\mathbf{\Omega}}^2 + \widetilde{\mathbf{\Omega}}^2\widetilde{\mathbf{S}} - \frac{2}{3} IV \mathbf{I}$

$\mathbf{T}^{(7)} = \widetilde{\mathbf{S}}^2\widetilde{\mathbf{\Omega}}^2 + \widetilde{\mathbf{\Omega}}^2\widetilde{\mathbf{S}}^2 - \frac{2}{3} V \mathbf{I}$

$\mathbf{T}^{(8)} = \widetilde{\mathbf{S}}\widetilde{\mathbf{\Omega}}\widetilde{\mathbf{S}}^2 - \widetilde{\mathbf{S}}^2\widetilde{\mathbf{\Omega}}\widetilde{\mathbf{S}}$

$\mathbf{T}^{(9)} = \widetilde{\mathbf{\Omega}}\widetilde{\mathbf{S}}\widetilde{\mathbf{\Omega}}^2 - \widetilde{\mathbf{\Omega}}^2\widetilde{\mathbf{S}}\widetilde{\mathbf{\Omega}}$

$\mathbf{T}^{(10)} = \widetilde{\mathbf{\Omega}}\widetilde{\mathbf{S}}^2\widetilde{\mathbf{\Omega}}^2 - \widetilde{\mathbf{\Omega}}^2\widetilde{\mathbf{S}}^2\widetilde{\mathbf{\Omega}}$

and β_k are scalar coefficients that are functions of five tensorial invariants

$$II_S = tr(\widetilde{\mathbf{S}}^2), \quad II_\Omega = tr(\widetilde{\mathbf{\Omega}}^2),$$

$$III_S = tr(\widetilde{\mathbf{S}}^3), \quad IV = tr(\widetilde{\mathbf{S}}\widetilde{\mathbf{\Omega}}^2),$$

$$V = tr(\widetilde{\mathbf{S}}^2\widetilde{\mathbf{\Omega}}^2).$$

Thus, equation 3.3 is the most generla formulation for τ^d in terms of $\tilde{S_{ij}}$ and $\tilde{\Omega_{ij}}$.

3.2 The dynamic procedure for EVM (DEVM)

Regarding to the model coefficient C_s for the eddy-viscosity model, it has been demonstrated that *a dynamic computation* of C_s (that is, during the simulation), can significantly improve the flow prediction accuracy.

The computation of C_s is done by taking into account the resolved scales, according to a scale invariance assumption.

The crucial point of this dynamic procedure is the so-called Germano identity. Let's now denote a test filter, $\widehat{\Delta} = 2\widetilde{\Delta}$, $\widetilde{\Delta} = \sqrt[3]{\Omega}$, where Ω is the volume of a computational cell. The Germano identity is defined as follows:

$$\mathscr{L}_{ij} = T_{ij} - \widehat{\tau}_{ij}, \tag{3.4}$$

where T_{ij} is the SGS stress tensor filtered at the test filter level, and $\mathscr{L}_{ij} = \widehat{\widetilde{u}_i\widetilde{u}_j} - \widehat{\widetilde{u}}_i\widehat{\widetilde{u}}_j$ Then $\mathscr{L}_{ij}$ is applied in this way:

$$\mathscr{L}_{ij} - \frac{1}{3}\mathscr{L}_{kk}\delta_{ij} = -2C_s\mathscr{M}_{ij} \tag{3.5}$$

where

$$\mathscr{M}_{ij} = \widehat{\Delta}^2|\widehat{\widetilde{S}}|\widehat{\widetilde{S}}_{ij} - \widetilde{\Delta}^2\widehat{|\widetilde{S}|\widetilde{S}_{ij}}. \tag{3.6}$$

The system of equations 3.5 is over-determined. In order to have a unique value of C_s Germano contracted it in:

$$C_s = -\frac{1}{2}\frac{\langle\mathscr{L}_{ij}\widetilde{S}_{ij}\rangle}{\langle\widetilde{S}_{ij}\mathscr{M}_{ij}\rangle} \tag{3.7}$$

Moreover, to make C_s variations smoother, a spatial averaging $\langle . \rangle$ has been applied.

Together with a better performance of the EVM, the Germano identity gives a correct asymptotic near-wall behaviour for ν_{SGS}.

It has also been shown that is possible to apply Germano identity for the dynamic computation of Pr_{SGS} in the EDM [Moin et al., 1991], improving performances in the scalar prediction.

3.3 Explicit Algebraic SGS stress model

Anisotropic effects of turbulence are important in several conditions: examples are near-wall flow behaviour and boundary layes separation cases with curvature, swirl, rotation.

As it was discussed before, the Dynamic Smagorinsky model is an isotropic model, in the sense that the SGS viscosity ν_{SGS} is direction-independent.

Therefore, in order to capture flow anisotropy, DEVM is not suitable.

In the same spirit as Reynolds stress-based models are necessary for RANS, non-linear SGS models are needed for LES.

A recent example of those is the nonlinear dynamic SGS stress model by Wang & Bergstrom [Wang and Bergstrom, 2005], which consists of three base tensors and three dynamic coefficients. One of the terms in the model is similar to the DEVM model. Wang & Bergstrom [Wang and Bergstrom, 2005] showed that the dynamic non-linear model predicts a more realistic tensorial alignment of the SGS stress than eddy-viscosity models and can provide for backscatter without clipping or averaging of the dynamic model parameters.

The model here discussed is called Explicit Algebraic SGS stress model (EASSM), was developed by Marstorp [Marstorp et al., 2009] and is similar to the EARSM by Wallin & Johansson [Wallin and Johansson, 2000], which is based on a modelled transport equation of the Reynolds stresses and on the assumption that the advection and diffusion of the Reynolds stress anisotropy are negligible.

Analogous to the Reynolds stress anisotropy tensor we define the SGS stress anisotropy tensor as

$$a_{ij} = \frac{\tau_{ij}}{K_{SGS}} - \frac{2}{3}\delta_{ij} \tag{3.8}$$

For simplicity, we'll consider $\tau_{ij}^{SGS} = \tau_{ij}$. Moreover, $K_{SGS} = (\widetilde{u_i u_i} - \widetilde{u}_i\widetilde{u}_i)/2$ is the SGS kinetic energy.

In a non-rotating frame the transport equation for a_{ij} reads

$$\underbrace{K_{SGS}\frac{Da_{ij}}{Dt}}_{advection} - \underbrace{\left(\frac{\partial D_{ijk}^{\tau_{ij}}}{\partial x_k} - \frac{\tau_{ij}}{K_{SGS}}\frac{\partial D_k^{K_{SGS}}}{\partial x_k}\right)}_{diffusion} = -\frac{\tau_{ij}}{K_{SGS}}(\mathcal{P}-\varepsilon) + \mathcal{P}_{ij} - \varepsilon_{ij} + \Pi_{ij}, \tag{3.9}$$

where $-D_k^{K_{SGS}} = -D_{ijk}^{\tau_{ij}}/2$ is the sum of the turbulent and molecular fluxes of the SGS stress and SGS kinetic energy, respectively.

Although the production of the SGS stress $\mathcal{P}_{ij}$ and SGS kinetic energy $\mathcal{P} = \mathcal{P}_{ii}/2$ are given in terms of τ_{ij} and filtered gradients, the SGS pressure strain Π_{ij} and SGS dissipation rate tensor ε_{ij}

need to be modelled. Those terms are

$$\mathcal{P}_{ij} = -\tau_{ik}\frac{\partial \widetilde{u}_j}{\partial x_k} - \tau_{jk}\frac{\partial \widetilde{u}_i}{\partial x_k} = K_{SGS}\left[-\frac{4}{3}\widetilde{S}_{ij} - (a_{ik}\widetilde{S}_{kj} + \widetilde{S}_{ik}a_{kj}) + (a_{ik}\widetilde{\Omega}_{kj} - \widetilde{\Omega}_{ik}a_{kj})\right], \tag{3.10}$$

$$\Pi_{ij} = \frac{2}{\rho}(\widetilde{S_{ij}p} - \widetilde{S}_{ij}\widetilde{p}), \tag{3.11}$$

$$\varepsilon_{ij} = 2\nu\left(\widetilde{\frac{\partial u_i}{\partial x_k}\frac{\partial u_j}{\partial x_k}} - \frac{\partial \widetilde{u}_i}{\partial x_k}\frac{\partial \widetilde{u}_j}{\partial x_k}\right) \tag{3.12}$$

and their modelling leads to [Launder et al., 1975]

$$\Pi_{ij} = -\varepsilon c_1 a_{ij} + K_{SGS}\left[\frac{3}{5}\widetilde{S}_{ij} + \frac{9c_2+6}{11}\left(a_{ik}\widetilde{S}_{kj} + \widetilde{S}_{ik}a_{kj} - \frac{2}{3}a_{km}\widetilde{S}_{mk}\delta_{ij}\right) + \frac{7c_2-10}{11}(a_{ik}\widetilde{\Omega}_{kj} - \widetilde{\Omega}_{ik}a_{kj})\right], \tag{3.13}$$

$$\varepsilon_{ij} = \varepsilon\frac{2}{3}\delta_{ij}, \tag{3.14}$$

where c_1 is a relaxation coefficient and $c_2 = 5/9$ is a parameter of the model for the rapid part of Π_{ij}, which depends directly on changes in the resolved velocity gradients, and $\varepsilon = \varepsilon_{ii}/2$.
Like in Wallin & Johansson's [Wallin and Johansson, 2000] RANS model, the derivation of the EASSM model involves the *weak equilibrium assumption*, which implies that the advection and diffusion terms of the Reynolds stress anisotropy are neglected. In order to simplify the model, together with the weak equilibrium assumption, we assume also that $\mathcal{P} = \varepsilon$. This leads to

$$0 = \mathcal{P}_{ij} - \varepsilon_{ij} + \Pi_{ij}. \tag{3.15}$$

Using the modelling given by 3.13 and 3.14 in 3.15 we have

$$c_1 a_{ij} = \tau^*\left[-\frac{11}{15}\widetilde{S}_{ij} + \frac{4}{9}(a_{ik}\Omega_{kj} - \Omega_{ik}a_{kj})\right] \tag{3.16}$$

note that $\tau^* = K_{SGS}/\varepsilon$ is the SGS time scale.
Finally, equation 3.16 has been solved using an *ansatz*

$$a_{ij} = \beta_1\tau^*\widetilde{S}_{ij} + \beta_4{\tau^*}^2(\widetilde{S}_{ik}\widetilde{\Omega}_{kj} - \widetilde{\Omega}_{ik}\widetilde{S}_{kj}), \tag{3.17}$$

where β_1 and β_4 are model parameters and functions of the filtered stress and strain-rate. Using that ansatz, equation 3.16 becomes

$$\tau_{ij} = K_{SGS}\left[\frac{2}{3}\delta_{ij} + \beta_1\tau^*\widetilde{S}_{ij} + \beta_4{\tau^*}^2(\widetilde{S}_{ik}\widetilde{\Omega}_{kj} - \widetilde{\Omega}_{ik}\widetilde{S}_{kj})\right], \tag{3.18}$$

which is the main EASSM model formulation. Using normalized strain and stress-rate tensors it can be rewritten as

$$\tau_{ij} = \frac{2}{3}\delta_{ij}K_{SGS} + \underbrace{\beta_1 K_{SGS}\widetilde{S}^*_{ij}}_{eddy-viscosity} + \underbrace{\beta_4 K_{SGS}(\widetilde{S}^*_{ik}\widetilde{\Omega}^*_{kj} - \widetilde{\Omega}^*_{ik}\widetilde{S}^*_{kj})}_{\substack{anisotropy\ of \\ SGS\ stresses}}. \tag{3.19}$$

The second term on the right-hand-side is an eddy viscosity term responsible for SGS dissipation, whereas the third term reproduces anisotropic effects of SGS stresses and gives a disalignment of the SGS stress and resolved strain-rate tensors. β_1 and β_4 coefficients have the form:

$$\beta_1 = -\frac{33}{20}\frac{9c_1/4}{[(9c_1/4)^2 + |\widetilde{\Omega}^*|^2]}, \qquad \beta_4 = -\frac{33}{20}\frac{1}{[(9c_1/4)^2 + |\widetilde{\Omega}^*|^2]} \tag{3.20}$$

where $|\widetilde{\Omega}^*| = \sqrt{2II^*_\Omega} = \sqrt{2\tau^{*2}\widetilde{\Omega}_{ik}\widetilde{\Omega}_{ki}} \leq 0$ is the SGS time scale-normalized second invariant. The unknown quantities K_{SGS} and τ^* can be dynamically or non-dynamically computed.

The equation 3.19 can also be related to the tensorial formulation of the SGS stress tensor, given in the previous section : the first term on the right-hand side reproduces the isotropic part of the SGS stress, while the second and third terms can be considered as two polynomial tensors, for the case $k = 1$ and $k = 4$.

The dynamic version of the EASSM involves Germano's dynamic procedure; here the SGS kinetic energy is modelled in terms of the squared Smagorinsky velocity scale $\Delta|\widetilde{S}_{ij}|$ [Yoshizawa, 1986]:

$$K_{SGS} = c\Delta^2|\widetilde{S}_{ij}|, \tag{3.21}$$

where $\widetilde{\Delta}$ is the filter scale; $|\widetilde{S}_{ij}| = (2\widetilde{S}_{ij}\widetilde{S}_{ij})^{1/2}$, and c is a dynamic parameter, computed in the following way:

$$\widehat{\widetilde{u}_i\widetilde{u}_i} - \widehat{\widetilde{u}}_i\widehat{\widetilde{u}}_i = c\widehat{\widetilde{\Delta}}^2 2\widehat{\widetilde{S}}_{ij}\widehat{\widetilde{S}}_{ij} - c\widetilde{\Delta}^2 2\widehat{\widetilde{S}_{ij}\widetilde{S}_{ij}}. \tag{3.22}$$

The quantities with $\widehat{\cdot}$ are test-filtered quantities. In this case the equation is not over-determined, because the number of filter operations needed for the dynamic constant computation is smaller than in DEVM.

Once c is computed, it is possible to obtain the coefficient c_1 and the SGS time scale τ^*:

$$c_1 = c_1' \sqrt{c_3'} \frac{c^{1.25}}{(2C_s)^{2.5}}, \qquad \tau^* = c_3' \frac{1.5 C_k^{1.5} \sqrt{c}}{2C_s} |\widetilde{S}|^{-1} \tag{3.23}$$

where $c_1' = 3.12$, $c_3' = 0.91$, $C_k = 1.5$ is the Kolmogorov constant and $C_s = 0.1$.

CHAPTER

4

IMPLEMENTATION IN A CFD CODE

"Patience is the companion of wisdom. (St.Augustine)"

In this chapter the implementation of the previous DEVM and EASSM models in a CFD code will be explained, together with a particular focus on pseudospectral methods and their features.

4.1 The need for accuracy: spectral methods

The aim of this thesis is to prove the effectiveness in prediction of the flow properties, given a specific turbulence model. In order to measure the accuracy of it, first we have to ensure that the only accuracy error that could be generated is given by the model, i.e. the accuracy is independent from the main code and the numerical method used. To fit this requirement, we need our code to have a numerical scheme which is not affected by numerical errors (e.g. truncation errors), therefore the use of the classic finite-difference (FD) method or finite-elements method (FEM) is not recommended for this purpose.
While finite-elements methods chop the interval in x into a number of sub-intervals, and choose the

$\phi_n(x)$ to be local functions which are polynomials of fixed degree, non-zero only over a couple of sub-intervals, spectral methods use global basis functions in which $\phi_n(x)$ is a polynomial of high degree which is non-zero over the entire computational domain, except at isolated points.
Once more, spectral methods, even if they generate algebraic equations with full matrices (in contrast with the FD, which uses sparse ones), *the high order of the basis functions gives high accuracy for a given number of degrees of freedom N.*
Despite spectral methods are the most useful when the geometry of the problem is fairly smooth and regular, when fast iterative matrix-solvers are used, spectral methods can be much more efficient than FEMs and FDs schemes. Therefore, for the case of channel flow, where the geometry is simple, they represents the best choice in terms of accuracy.

4.1.1 Accuracy and memory saving properties

Finite difference methods approximate the unknown $u(x)$ by a sequence of overlapping polynomials which interpolate $u(x)$ at a set of grid points. The derivative of the local interpolant is used to approximate the derivative of $u(x)$. The result consists of a weighted sum of the values of $u(x)$ at the interpolation points. The following picture shows how the polynomials are in the different methods.

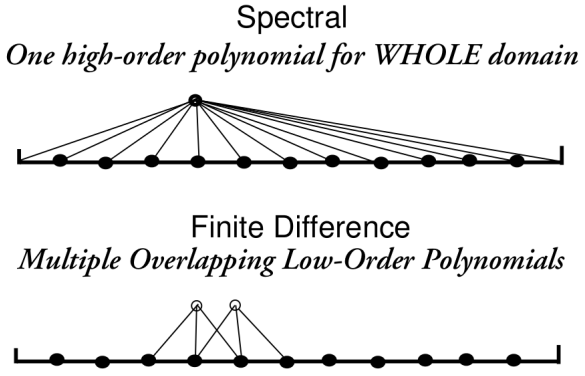

Figure 4.1 – Spectral methods and finite difference schemes

To ensure a computational ease, together with completeness and rapid convergence of the solution, there are several alternatives for the choice of the basis functions.
One of the best combinations used is to employ Fourier series in x and z directions, where the solution is assumed to be periodic; along the y direction, instead, the solution won't be periodic, and Chebychev polynomials represents the best *disguise* for a spectral method [Boyd, 2001] there. For this reason, a code with such combination like this one is called a *Pseudo-Spectral* method.

Let's consider now a 3-points FD method (like a second-order one), and a N-point pseudo-spectral method. It has been proved that, to equal the accuracy of the pseudospectral procedure for $N = 10$, one would need a 10^{th} order finite difference or FEM with a $\mathcal{O}(h^{10})$ error.
Increasing N, the pseudospectral method have two positive aspects: the interval h between grid point becomes smaller, and the error rapidly decreases even if the order of the method is fixed; which is not true, since the order of the method is *not fixed*. The combination of these two aspects makes this method extremely efficient: passing from $N = 10$ to $N = 20$, the error becomes $\mathcal{O}(h^{20})$, with also a new smaller h, since h is $\mathcal{O}(1/N)$. Summarizing it holds that

$$\text{Pseudospectral error} \approx \mathcal{O}[(1/N)^N]$$

which means that the error decreases faster than any finite power of N because the power in the error formula is always increasing, too. We can describe this behaviour as *infinite order* or *exponential* convergence. This feature makes the pseudospectral method the best choice when many decimal places of accuracy are needed.
This is not the only one benefit of using spectral method, though. Pseudospectral methods are also *memory-minimizing*, this means that the number of degrees of freedom required in each dimension by them are about half as the ones needed by a fourth-order FD method. This leads to the fact that high-resolution problems could be solved satisfactorily by spectral methods, when a three-dimensional second order FD code would fail because of the need for eight or ten times as many grid points would exceed the core memory of the available computer.

4.2 The SIMSON code

To perform the LES, the SIMSON code has been used. SIMSON is a pseudo-Spectral Solver for IncoMpreSsible bOuNdary layer flows, developed by Chevalier [Chevalier et al., 2007]. In Simson channel and boundary layer solvers have been combined together with many additional features developed over the years. The code can compute either direct numerical simulations (DNSs) or large-eddy simulations (LESs); in LES mode, different subgrid-scale models are available, including the DEVM. The EASSM has been recently implemented.
The code is completely written in Fortran 75/90 and can be run with distributed or with shared memory parallelization using the Message Passing Interface (MPI) or OpenMP.
The wall-parallel directions are discretized using Fourier series and the wall-normal direction using Chebyshev series. Time integration is performed using a third order Runge-Kutta method for the advective and forcing terms, and a Crank-Nicolson method for the viscous terms.

4.2.1 Theory

The SIMSON code is an incompressible Navier-Stokes solver. In a rotating reference frame, N-S equations are, written in tensor notation:

$$\frac{\partial u_i}{\partial t} = -\frac{\partial p}{\partial x_i} + \epsilon_{ijk} u_j (\omega_k + 2\Omega_k) - \frac{\partial}{\partial x_i}\left(\frac{1}{2} u_j u_j\right) + \frac{1}{Re}\nabla^2 u_i + F_i, \qquad \frac{\partial u_i}{\partial x_i} = 0. \tag{4.1}$$

where $(\omega_1, \omega_2, \omega_3) = (\chi, \omega, \vartheta)$ are the vorticities along streamwise, wall-normal and spanwise coodinates. Ω_k is the angular velocity of the coodinate frame around axis k. The body force $\mathbf{F} = (F_1, F_2, F_3)$ is used for numerical purposes and to introduce external disturbances to the flow. Taking the divergence of the momentum equations we derive the Poisson equation for the pressure

$$\nabla^2 p = \frac{\partial}{\partial x_i} \underbrace{[\epsilon_{ijk} u_j (\omega_k + 2\Omega_k) + F_i]}_{H_i} - \nabla^2\left(\frac{1}{2} u_j u_j\right) \tag{4.2}$$

Applying the Laplace operator to the momentum equations for the wall-normal velocity one finds

$$\frac{\partial \nabla^2 v}{\partial t} = \left(\frac{\partial^2}{\partial x^2} + \frac{\partial^2}{\partial z^2}\right) H_2 - \frac{\partial}{\partial y}\left(\frac{\partial H_1}{\partial x} + \frac{\partial H_3}{\partial z}\right) + \frac{1}{Re}\nabla^2 v \tag{4.3}$$

for numerical purposes, this equation can be rewritten as a system of equations:

$$\begin{cases} \frac{\partial \phi}{\partial t} = h_v + \frac{1}{Re}\nabla^2 \phi \\ \nabla^2 v = \phi, \end{cases} \tag{4.4}$$

where

$$h_v = \left(\frac{\partial^2}{\partial x^2} + \frac{\partial^2}{\partial z^2}\right) H_2 - \frac{\partial}{\partial y}\left(\frac{\partial H_1}{\partial x} + \frac{\partial H_3}{\partial z}\right) \tag{4.5}$$

Moreover, taking the curl of the momentum equations, an equation for the normal vorticity can be derived as well:

$$\begin{cases} \frac{\partial \omega}{\partial t} = h_\omega + \frac{1}{Re}\nabla^2 \omega \\ h_\omega = \frac{\partial H_1}{\partial z} - \frac{\partial H_3}{\partial x} \end{cases} \tag{4.6}$$

The system of equation above can be solved with the same numerical routine. Once the normal velocity v and vorticity ω have been calculated, the other velocity components can be computed from the incompressibility constraint and the wall-normal vorticity definition.

4.2.2 Numerical method

Time discretization. The time discretization used by Simson can be explained using the following equation:

$$\frac{\partial \psi}{\partial t} = G + L\psi \tag{4.7}$$

ψ represents ϕ or ω. L is the linear diffusion and is implicitly discretized by a Crank-Nicolson (CN) scheme, while G is explicitly discretized by a third order three or four stage Runge-Kutta (RK3) scheme. The overall time discretization can be shown in the following way

$$\psi^{n+1} = \psi^n + a_n G^n + b_n G^{n-1} + (a_n + b_n)\left(\frac{L\psi^{n+1} + L\psi^n}{2}\right), \tag{4.8}$$

where a_n and b_n are constants chosen according to the explicit scheme.

Using the scheme 4.8 in 4.7, the previously written equations become:

$$\begin{cases} \left(1 - \frac{a_n+b_n}{2Re}\nabla^2\right)\phi^{n+1} = \left(1 + \frac{a_n+b_n}{2Re}\nabla^2\right)\phi^n + a_n h_v^n + b_n h_v^{n-1}, \\ \nabla^2 v^{n+1} = \phi^{n+1}, \end{cases} \tag{4.9}$$

and

$$\left(1 - \frac{a_n+b_n}{2Re}\nabla^2\right)\omega^{n+1} = \left(1 + \frac{a_n+b_n}{2Re}\nabla^2\right)\omega^n + a_n h_\omega^n + b_n h_\omega^{n-1}. \tag{4.10}$$

Horizontal discretization. The horizontal discretization has been made using a Fourier expansion, assuming that the solution is periodic. Each variable is assumed to be spanwise and streamwise-dependent, that is

$$u(x,z) = \sum_{l=-(\frac{N_x}{2}-1)}^{\frac{N_x}{2}-1} \sum_{m=-(\frac{N_z}{2}-1)}^{\frac{N_z}{2}-1} \widehat{u}(\alpha_l, \beta_m) e^{i(\alpha_l x + \beta_m z)} \tag{4.11}$$

where $\alpha_l = 2\pi l / x_L$ and $\beta_m = 2\pi m / z_L$ and N_x and N_z are the number of Fourier modes in the two directions. Note that $k^2 = \alpha^2 + \beta^2$. Using this discretization the equations 4.9 can be rewritten as

$$\begin{cases} \left(1 - \frac{a_n+b_n}{2Re}(D^2 - k^2)\right)\widehat{\phi}^{n+1} = \left(1 + \frac{a_n+b_n}{2Re}(D^2 - k^2)\right)\widehat{\phi}^n + a_n \widehat{h}_v^n + b_n \widehat{h}_v^{n-1}, \\ (D^2 - k^2)\widehat{v}^{n+1} = \widehat{\phi}^{n+1}, \end{cases} \tag{4.12}$$

where D stands for the derivative in wall-normal direction.

Wall-normal discretization. The normal discretization has been done through Chebychev's polynomials. Using an example of second order constant coefficient ordinary differential equation

$$(D^2 - \kappa)\widehat{\psi} = \widehat{f}, \quad \widehat{\psi}(0) = \gamma_{-1}, \quad \widehat{\psi}(y_L) = \gamma_1. \tag{4.13}$$

This is solved expanding ψ, its second derivative, $\widehat{f}$ and the boundary conditions in Chebychev series:

$$\widehat{\psi}(y) = \sum_{j=0}^{N_y} \widetilde{\psi}_j T_j(y), \tag{4.14}$$

$$D^2\widehat{\psi}(y) = \sum_{j=0}^{N_y} \widetilde{\psi}_j^{(2)} T_j(y), \tag{4.15}$$

$$\widehat{f}(y) = \sum_{j=0}^{N_y} \widetilde{f}_j T_j(y), \tag{4.16}$$

$$\widehat{\psi}(1) = \sum_{j=0}^{N_y} \widetilde{\psi}_j = \gamma_1, \tag{4.17}$$

$$\widehat{\psi}(-1) = \sum_{j=0}^{N_y} (-1)^j \widetilde{\psi}_j = \gamma_{-1}, \tag{4.18}$$

where T_j are the Chebychev polynomials of order j and N_y the highest order of polynomial included in the expansion.

Non-linear terms. Non-linear terms of LES equation, $\tilde{u}_j \frac{\partial \tilde{u}_i}{\partial x_j}$, are known to be computationally expensive anyhow. Despite the computation of the whole velocity field is performed in a Fourier space through Fast Fourier Trasforms (FFTs), i.e. in the complex space ($\mathbb{C}$), the non-linear terms are calculated coming back to real space, $\mathbb{R}$. Then the following computation will be finished in Fourier space.

4.2.3 MPI parallelization

An important process able to boost performances of the CFD code and decrease computational time is the parallelization of the code.
In serial computations the problem is broken into a discrete series of instructions, which are executed sequentially one after another on a single processor.

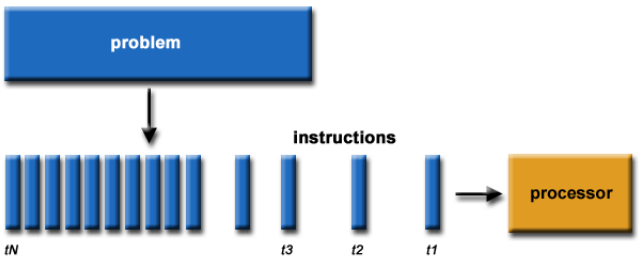

Figure 4.2 – Serial computation scheme

Different from serial runnings, in parallel computing:

- A problem is broken into discrete parts that can be solved concurrently;
- Each part is further splitted in to a series of instructions;
- Instructions from each part execute simultaneously on different processors;
- each processor send/receive information to/from the other ones through MPI communication, therefore
- An overall control/coordination mechanism is employed.

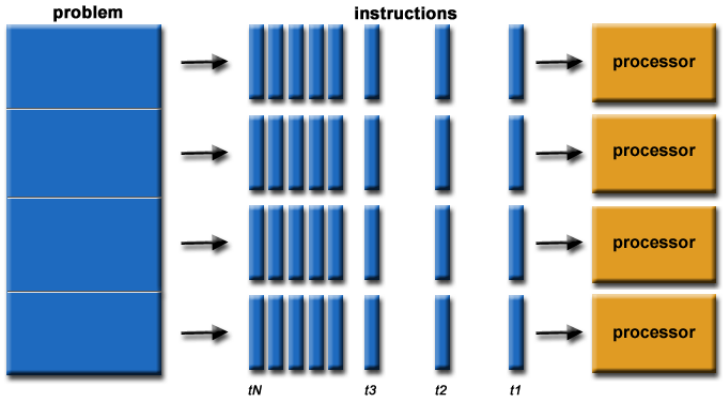

Figure 4.3 – Parallel computation scheme

For parallelization purposes, the computational problem should be able to be broken apart into discrete pieces of work that can be solved simultaneously, and execute multiple program instructions at any moment in time. Of course, the problem is expected to be solved in less time with multiple compute resources than with a single compute resource. Typically, compute resources can be either a single computer with multiple processors/cores or an arbitrary number of such computers connected by a network. There's also a way to quantify how much computational time can be saved using parallel computing. Amdahl's Law states that potential program speedup is defined by the fraction of code (P) that can be parallelized:

$$speedup = \frac{1}{1-P} \tag{4.19}$$

If none of the code can be parallelized, $P = 0$ and the $speedup = 1$ (no speedup), while if all of the code is parallelized, $P = 1$ and the speedup is infinite (in theory).
If 50% of the code can be parallelized, $speedup_{max} = 2$, meaning the code will run twice as fast.
Introducing the number of processors performing the parallel fraction of work, the relationship can be modeled by:

$$speedup = \frac{1}{P/N + S} \tag{4.20}$$

where P is the parallel fraction, N the number of processors and S the serial fraction.
The diagrams in the next page show how parallelization improves performances in terms of *speedup*.

4.2.3.1 MPI communication between processes

Once the problem has been splitted into several processors, the necessity of coomunication between processes occurs. In other words, we need processors to send and receive data between them, in order to run a distributed simulation.
Communication occurs when a portion of one process' address space is copied into another process' address space. This operation is cooperative and occurs only when the first process executes a *send* operation and the second process executes a *receive* operation. On the sender's side, the way to describe data is to specify a starting address, a length of the message (in bytes), the destination address, and a tag. The tag is needed for the matching between messages, it is an information (an integer) to let the process control which messages it receives.
On the other side, the receiver will need to receive the address and the length of the place the data has to be placed, together with the tag, the source and the length of the message received. The message interface therefore will be:
`send (address, length, destination, tag)`
and
`recv (address, length, source, tag, actlen)`.

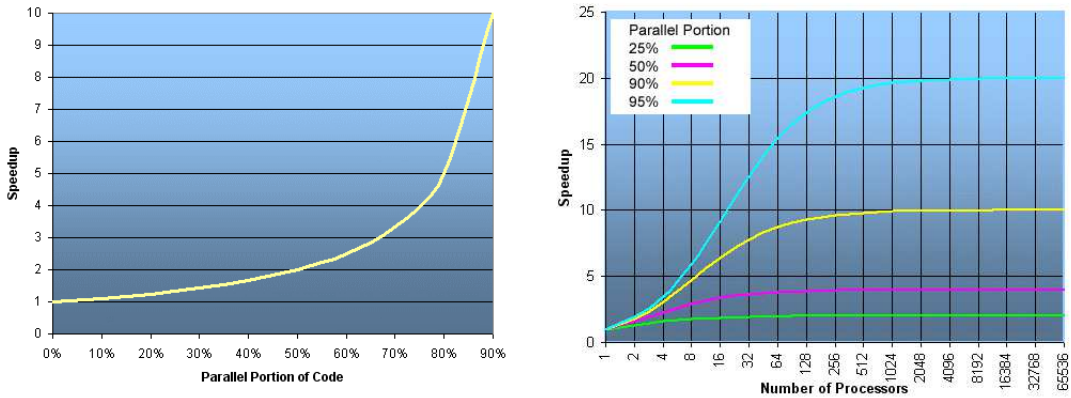

Figure 4.4 – Parallel computing performances diagrams [Laure, 2014]

In SIMSON code parallelization is made using Message-Passing Interface protocol. In particular, what MPI parallelization does is to split the computational grid into several parts, equal to the number of available processors; then every CPU processor (or core) computes its part at the same time. There are several ways the computational domain can be split to; however the most

common ones are 1D parallelization and 2D parallelization. In the following simulations both of the parallelization methods are used; in the figure below both types of them are shown.

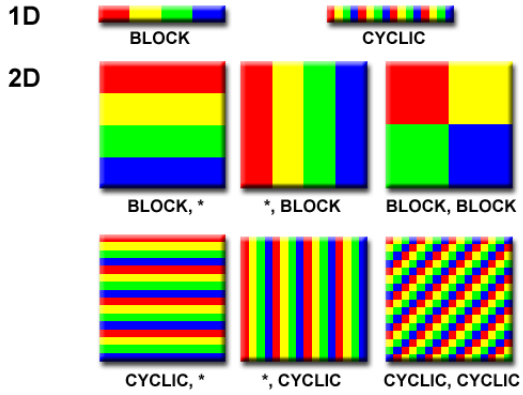

Figure 4.5 – Parallel computing distributions [Gropp et al., 1999]

In this work two versions of SIMSON code have been used. The former one is 1D parallelized, therefore the domain is splitted in rectangular processors, only in 1 direction, which is along the z axis (configuration `CYCLIC,*`) .

The latter one is the 2D parallelization: in SIMSON code it involves the domain splitting in x (`nprocx` is the number of processors in that direction) and z (`nprocz`) and the total number of processes is then `nproc = nprocx * nprocz`. Therefore the `BLOCK,BLOCK` configuration has been implemented.

To carry on simulations, several supercomputers that belong to the Swedish National Infrastructure for Computing (SNIC) will be used. For the last and more time-consuming simulation, Lindgren supercomputer will be employed. A photo of it is shown below.

Figure 4.6 – Lindgren supercomputer at PDC, KTH

CHAPTER

5

POSTPROCESSING TOOLS FOR TURBULENCE

"However difficult life may seem,
there is always something you can do and succeed at. (S. Hawking)"

Once the simulation has been run, the output generated is a turbulent velocity field, and has to be postprocessed using several tools; some of them come from statistical analysis. The results are the mean values, two-point time statistics, i.e. correlations, and the so-called vortical structures.

5.1 Mean Values

The simplest statistical property is the mean value, or first moment. The mean value of a random variable at a particular spatial location can be derived by averaging the long time measurement of that variable. Considering the measurement period T we have:

$$\langle u \rangle = \lim_{T \to \infty} \frac{1}{T} \int_{t_0}^{t_0+T} u(t) dt. \tag{5.1}$$

where $\langle u \rangle$ indicates the mean value of a random variable u (the flow velocity in this case), and t_0 is the measurement starting time. This time average only makes sense if 5.1 is independent of t_0 and T for large T; in this case we would say that *the integral converges* and the flow can be assumed as *statistically steady* and therefore is meant as a *stationary process*.
However, this integral doesn't converge in some situations. In such cases the mean flow behaviour can be described by the *ensemble average*, which is taken on a finite volume V, and defined as:

$$\langle u \rangle = \lim_{V \to \infty} \frac{1}{V} \int_{V} u(\mathbf{x}) dx dy dz. \tag{5.2}$$

The integration is therefore performed over a volume at one instant of time. Note that the previous relation holds only if the flow is spatially-independent. In a discrete volume domain we can refer to a number of samples, N, and the equation 5.3 becomes

$$\langle u \rangle = \lim_{N \to \infty} \frac{1}{N} \sum_{1}^{N} u(x). \tag{5.3}$$

Since we will consider a fully-developed flow, in our specific case we will assume the mean value as the quantity of the flow which is averaged both in time, and space. Thus, the flow will be assumed to be statistically stationary, i.e. mean velocities keep constant along the x and z-axis.

5.2 Root-mean squared Values, rms

Turbulence has to be quantified also in its strength. In turbulence, the root-mean squared operation consists in the square root of the of the mean value of the squared of the velocity fluctuations, u_i':

$$u_{i,rms} = \sqrt{\langle u_i'(t)^2 \rangle} \tag{5.4}$$

on a discrete domain

$$u_{i,rms} = \sqrt{\frac{1}{N} \sum_{i=1}^{N} (u_i')^2} \tag{5.5}$$

5.3 Vortical structures

Up to now we have described turbulence in a statistical way. However, a useful method to analyze vortical structures is well appreciated.

Between different methods that have been developed during the past years, we can find several criteria to identify vortices, but the most precise and coherent one is the λ_2 structures method.

According to the paper of Jeong & Hussain [Jeong and Hussain, 1995], the λ_2 method uses the strain and rotation-rate tensors to determine the existence of a local pressure minimum due to vortical motion; the *vortex core is defined as a connected region with two negative eigenvalues of* $\mathbf{S}^2 + \mathbf{\Omega}^2$.

Since $\mathbf{S}^2 + \mathbf{\Omega}^2$ is a symmetric tensor, it has only real eigenvalues.

Calling the eigenvalues λ_1, λ_2 and λ_3, with $\lambda_1 \geq \lambda_2 \geq \lambda_3$, the requirement for a pressure minimum is that $\lambda_2 < 0$ within the vortex core. In particular,

$$tr(\mathbf{S}^2 + \mathbf{\Omega}^2) = \lambda_1 + \lambda_2 + \lambda_3. \tag{5.6}$$

Considering a general velocity gradient for a planar flow:

$$\nabla \mathbf{u} = \begin{pmatrix} a & b \\ c & -a \end{pmatrix} \tag{5.7}$$

which can be rewritten in

$$\mathbf{S}^2 + \mathbf{\Omega}^2 = \begin{pmatrix} a^2 + bc & 0 \\ 0 & a^2 + bc \end{pmatrix} \tag{5.8}$$

λ_2 is the second eigenvalue of that tensor. The condition previous cited requires that $\lambda_2 < 0$, therefore $a^2 + bc < 0$.

CHAPTER

6

RESULTS

"Continuous effort - not strength or intelligence - is the key to unlocking our potential.
(W.Churchill)"

In this chapter results of several LES at different Re_τ will be analyzed. The substantial differences between DEVM and EASSM model will be commented upon and special attention will be paid to anisotropy effects of the latter model. In all the simulations, the flow domain is a rectangular box. Streamwise and spanwise dimensions are varied with the friction Reynolds number. A sketch of the flow domain is shown in figure 6.1

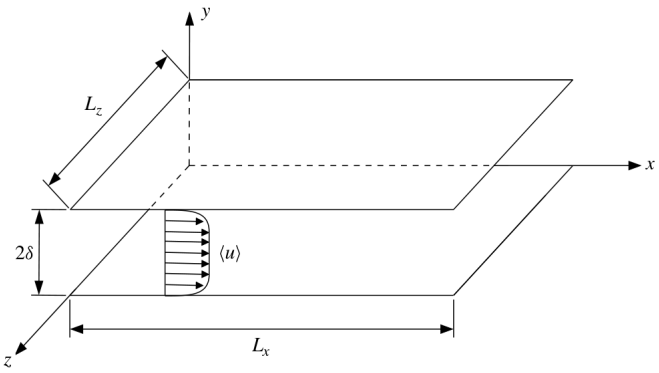

Figure 6.1 – Sketch of the flow domain used for LESs.

The resolution of the LES is defined in terms of grid spacings; Δ_x^+, Δ_y^+, Δ_z^+ are the grid spacings in physical space in streamwise, wall-normal and spanwise directions respectively, in wall units; in x and z directions they are defined as

$$\Delta_x^+ = \frac{l_x}{N_x} Re_\tau, \qquad \Delta_z^+ = \frac{l_z}{N_z} Re_\tau \tag{6.1}$$

where N_x and N_z are the number of Fourier modes, l_x and l_z the lengths of the computational box, in x and z directions, and Re_τ is the Reynolds number based on friction velocity.
The following simulations were started using an initial field, generated with random fluctuations. Then they have been run for some time, in order to reach a statistically stationary state. Once the simulations have been finished, statistics of the flow has been collected for a certain time period.

6.1 LES at $Re_\tau = 590$

In this section LES results of turbulent channel flow at the bulk Reynolds number corresponding to the DNSs of Moser & Kim at $Re_\tau = 590$, are presented. In order to show anisotropic effects of the EASSM, the related results have been compared with the isotropic DEVM model. Three cases, with ascending order of resolution, are presented. For these simulations,a computational box with a streamwise and spanwise size of $2\pi\delta$ and $\pi\delta$ respectively, where δ is the channel half width, has been chosen. The bulk Reynolds number is $Re_b = \overline{u}\delta/\nu = 10935$ and the friction Reynolds number is $Re_\tau = 593$ in the DNS.
The parameters of the LES are given in table 6.1. Since Re_b in the LESs is the same as in the DNS, Re_τ can vary. The table shows that Re_τ depends on the SGS model and the resolution.

Table 6.1 – Channel Flow simulations, for $Re_\tau = 590$. The first three cases have been computed with the Dynamic Smagorinsky model (DEVM) while the latter ones refer to the explicit algebraic SGS model (EASSM). N_x, N_y, N_z are the numbers of Fourier modes in the streamwise, wall-normal and spanwise directions, respectively. $\Delta_{y^+,min}$ and $\Delta_{y^+,max}$ are the minimum and maximum grid spacings in wall-normal direction. $\tau_w/\tau_{w,DNS}$ is the ratio between the wall shear stress given by the LES and the one from DNS.

Case	**SGS model**	$N_x \times N_y \times N_z$	Δ_x^+	Δ_z^+	$\frac{\Delta_y^+}{min \sim max}$	Re_τ	$\frac{\tau_w}{\tau_{w,DNS}}$
DS0	DEVM	$64 \times 65 \times 64$	58	29	$0.68 \sim 27.69$	564	0.92
DS1	DEVM	$96 \times 97 \times 72$	38	25	$0.31 \sim 18.91$	578	0.97
DS2	DEVM	$128 \times 97 \times 96$	29	19	$0.31 \sim 18.91$	583	0.99
EA0	EASSM	$64 \times 65 \times 64$	57	29	$0.70 \sim 28.65$	584	0.99
EA1	EASSM	$96 \times 97 \times 72$	39	26	$0.32 \sim 19.47$	595	1.03
EA2	EASSM	$128 \times 97 \times 96$	29	19	$0.31 \sim 19.20$	587	1.00

Table 6.2 – Channel Flow simulations for $Re_\tau = 590$. MPI parallelization details. The first three cases have been computed with the Dynamic Smagorinsky model (DEVM) while the latter ones refer to the explicit algebraic SGS model (EASSM)

Case	**SGS model**	n (no. processors)	N (no. nodes)	Supercomputer
DS0	DEVM	16	2	Abisko
DS1	DEVM	16	2	Abisko
DS2	DEVM	12	1	Povel
EA0	EASSM	12	1	Povel
EA1	EASSM	16	1	Povel
EA2	EASSM	16	1	Povel

Convergence criterion. In order to obtain reliable results, the convergence of the solution has been checked in two ways:

1. the stationarity of the turbulent kinetic energy;
2. the approach to steady-state of the total shear stress.

After several time units, $t = 2000$, the diagram below ensures the steady-state of the solution, since the total shear stress assumes the shape of a perfectly-straight line.

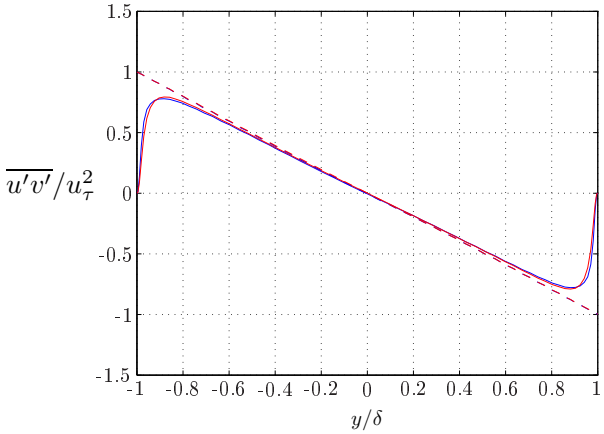

Figure 6.2 – Deviatoric part of the Reynolds stress profile in wall units, together with the total shear stress (in dashed line). —— : EA0 – – : DS0

Resolution study. Before investigating the main characteristics of the flow, an important aspect to look at is the effect of the spatial resolution, which can be checked by studying the ratio between the friction at the wall for the LES case and the one for the DNS case, i.e. $\tau_{wall}/\tau_{wall,DNS}$. This ratio can be readily derived from the Re_τ of each case,

$$\frac{\tau_{wall}}{\tau_{wall,DNS}} = \frac{\rho u_\tau^2}{\rho u_{\tau,DNS}^2} = \frac{Re_\tau^2}{Re_{\tau,DNS}^2} \tag{6.2}$$

This value should be one is the LES perfectly agrees with DNS.

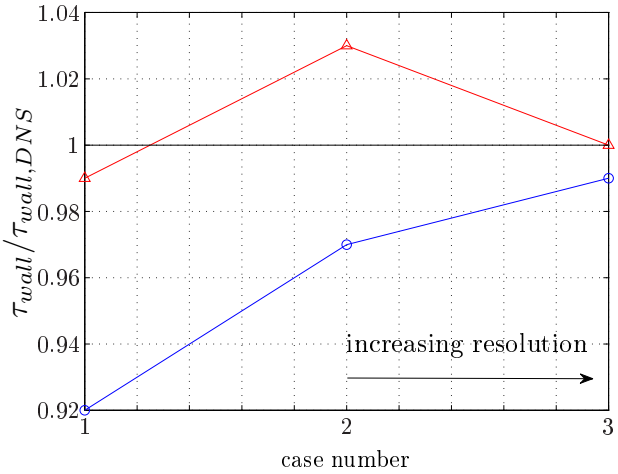

Figure 6.3 – Variation of averaged wall shear stress, normalized with the DNS value, with resolution. $-\triangle-$: EASSM cases, $-\bigcirc-$: DEVM cases, $-$: DNS

From figure 6.3 we can see the different trends of the two models adopted. While the DEVM gives a monotonic behaviour as the resolution increases, the EASSM convergence of the τ_{wall} towards the DNS profile is not monotonic. Overall the EASSM gives the best predictions in comparison with the DNS.

Profiles. The mean velocity profiles are shown in figure 6.22. EASSM predictions are clearly more accurate than DEVM at any resolution; the difference in results becomes remarkable as soon as we go further from the inner region and we approach the outer layer, towards the centreline. The DEVM overpredicts the mean velocity profile at coarser resolutions, while EASSM approaches fairly well the DNS velocity profile also at the coarsest resolution.

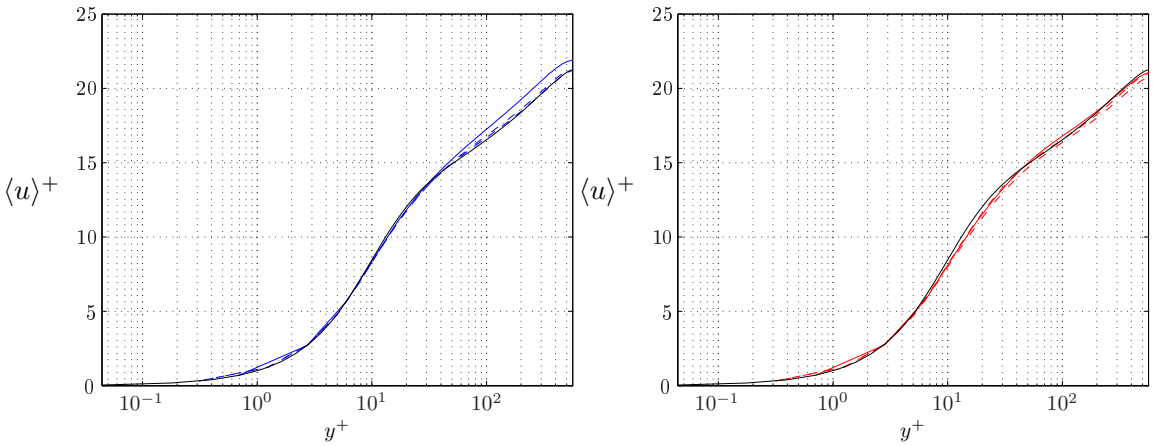

Figure 6.4 – Mean velocity profiles in wall units at increasing resolutions. – : EA0, – · – : EA1, – – : EA2, – : DS0, – · – : DS1, – – : DS2. – : DNS

The components of Reynolds stress tensor are shown in figure 6.5. The presence of the walls and the shear forces the flow to be highly anisotropic. Therefore, fluctuations along streamwise direction are much bigger than in the wall-normal and spanwise directions. Here the DEVM shows a good prediction of the u' component, while the estimation of the other components v' and w' is quite inaccurate compared to the EASSM. This is reasonable, since the DEVM is an isotropic model and doesn't properly model the SGS anisotropy.

By contrast, we can conclude that the EASSM gives a good prediction of the anisotropy, which is well modelled through the SGS model. A close-up of the deviatoric component of the Reynolds stress profile is shown in figure 6.6. Both models seem to give a good performance. The effects of increasing resolution are highlighted in the figure: the arrow points to ascending resolution cases.

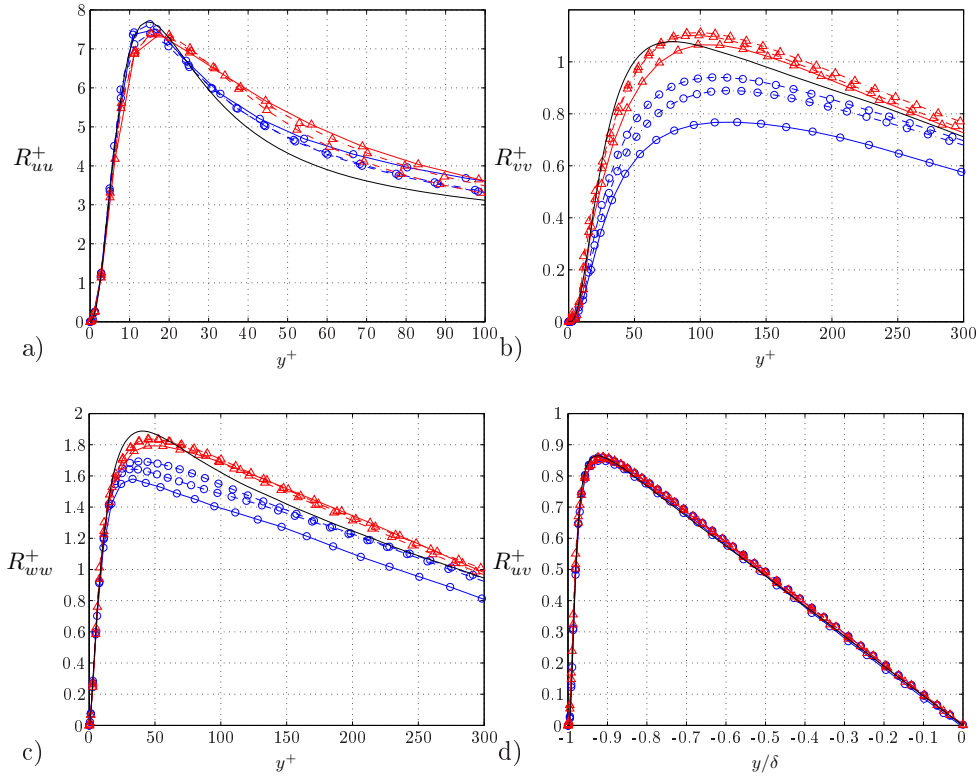

Figure 6.5 – Reynolds stress components profiles in wall units at different resolutions.
– : EA0, –·– : EA1, –– : EA2, – : DS0, –·– : DS1, –– : DS2, – : DNS.

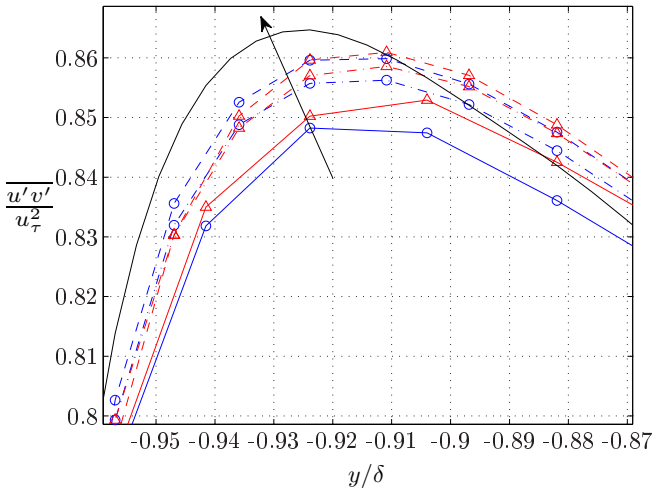

Figure 6.6 – Reynolds shear stress profile in wall units at increasing resolutions.
–△– : EA0, –·△–·– : EA1, ––△–– : EA2, –◯– : DS0, –·◯–·– : DS1, ––◯–– : DS2, – : DNS

The following diagram shows that EASSM and DEVM have a similar prediction also of the ratio turbulence production $\mathcal{P}$ and the turbulent dissipation ε, and they present results close to DNS. Regarding EASSM, an important aspect to remark is the $\mathcal{P} = \varepsilon$ assumption in the SGS model. However, this assumption is not valid for the resolved scales.

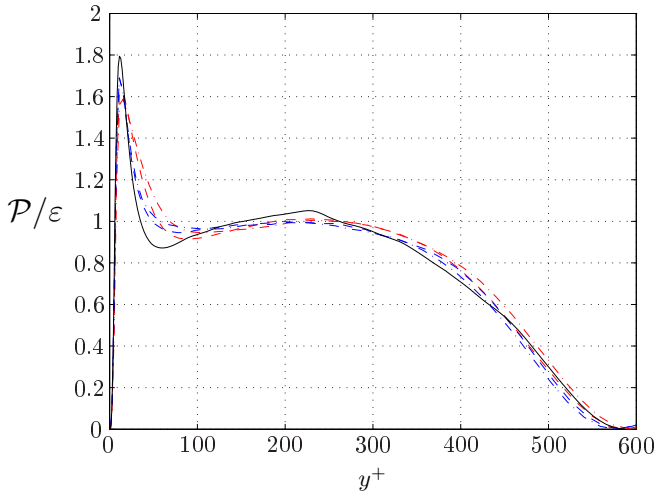

Figure 6.7 – Turbulent production-dissipation ratio at increasing resolutions. – · – : EA1, – – : EA2, – · – : DS1, – – : DS2, – : DNS

SGS Anisotropy effects. Let's perform now a deep analysis of the contribution of the sub-grid scale model to prediction performance. First of all, a distinction between the resolved quantities and the SGS ones must be defined. In order to focus on anisotropy prediction, we will analyze the deviatoric part of the Reynolds stress. Let's call the resolved part of this quantity $\tau_{12}^{r,+}$, and the SGS contribution (given by the specific model), $\tau_{12}^{SGS,+}$. Therefore, the total prediction of the quantity will be

$$\tau_{12}^{+} = \tau_{12}^{r,+} + \tau_{12}^{SGS,+} \tag{6.3}$$

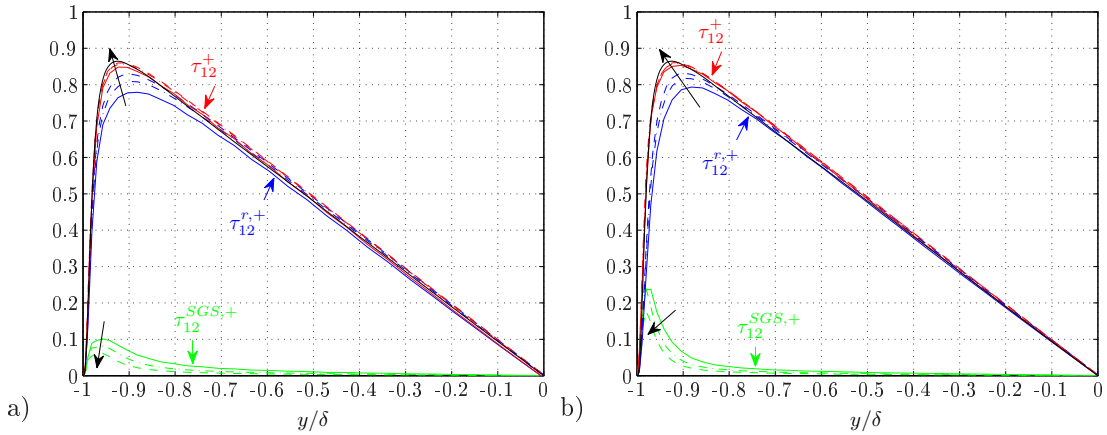

Figure 6.8 – Deviatoric part of the Reynolds stress profile in wall units, a) with DEVM model b) with EA model. Black arrows point at increasing resolutions. – : DNS

From the figures above we can note an important aspect of the SGS models: at increasing resolutions, the SGS prediction decreases, while the resolved part increases. This is reasonable: the finer the resolution is, the larger the range of resolved scales will be. Therefore, the SGS contribution will become smaller with increasing resolution. Vice versa, at the smallest resolution we can analyze the performances of each model: EASSM gives the best prediction, its contribution is larger than DEVM, and is a superior model for the quality of the flow predictions given.

Flow visualizations. Some flow visualizations of the fluctuating flow field have been carried out in order to capture the elongated structures (streaks), which have been generated by the influence of the wall shear stress at a very small distance from the wall. LES results are compared with DNS (by a courtesy of P.Schlatter), at the same friction Reynolds number.
Although the description of the streaks is not that detailed, LES with the EASSM model is able to capture some of this particular structures at the wall. On the other hand, DNS gives a complete description and the flow is perfectly described since a wider range of scales have been computed. The streaks are only seen in the visualizations of the streamwise velocity field; in the visualizations of the other two velocity components the streaks are absent.

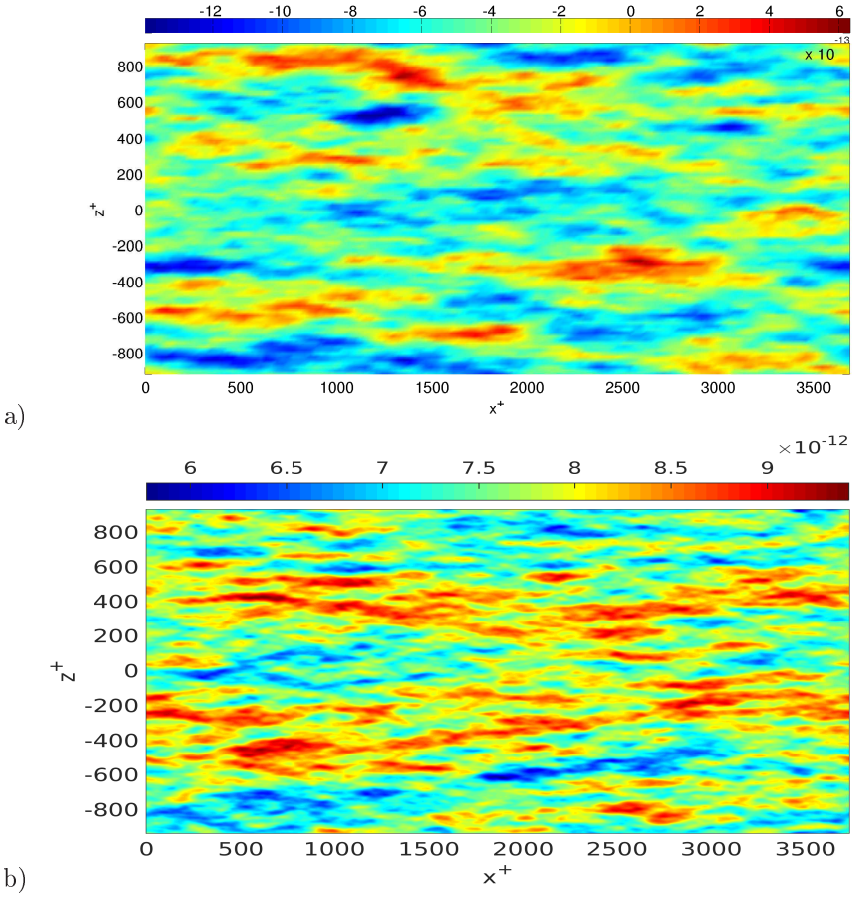

Figure 6.9 – Horizontal contour plots of streamwise fluctuations u'^+ at $y^+ \approx 8$, along the xz plane, a) simulation EA2, b) DNS by P.Schlatter.

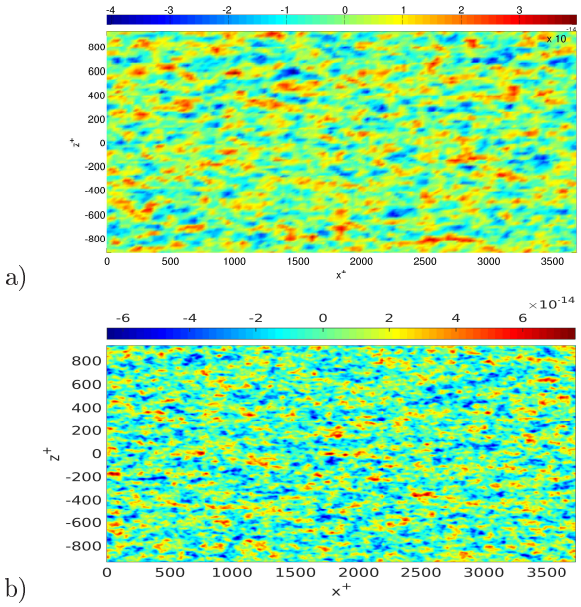

Figure 6.10 – Horizontal contour plots of wall-normal fluctuations v'^+ at $y^+ \approx 8$, along the xz plane, simulation EA2, b) DNS by P.Schlatter.

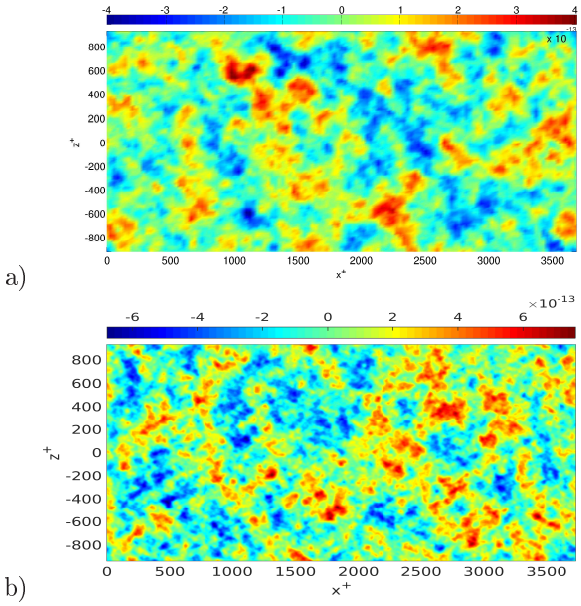

Figure 6.11 – Horizontal contour plots of spanwise fluctuations w'^+ at $y^+ \approx 8$, along the xz plane, simulation EA2, b) DNS by P.Schlatter.

6.2 LES at $Re_\tau = 2000$

Let's study now a higher Re_τ case. In this section LES of a channel flow at the bulk Reynolds number corresponding to the DNSs of Jiménez et al (2006) of $Re_\tau = 2000$, are presented.
For this case two simulations have been carried out, one with the DEVM and the other with EASSM, with a computational box $5\pi\delta$ long in streamwise direction and $2\pi\delta$ long in spanwise direction. The bulk Reynolds number is $Re_b = 43466$ and the DNS friction Reynolds number is $Re_\tau = 2003$. Details of these simulations are shown in table 6.3.

Table 6.3 – Channel Flow simulations, for $Re_\tau = 2000$. The first case has been computed with the Dynamic Smagorinsky model (DEVM) while the latter one refers to the explicit algebraic SGS model (EASSM)

Case	SGS model	$N_x \times N_y \times N_z$	Δ_x^+	Δ_z^+	$\frac{\Delta_y^+}{min \sim max}$	Re_τ	$\frac{\tau_w}{\tau_{w,DNS}}$
DS	DEVM	$160 \times 193 \times 160$	180	72	$0.25 \sim 30.04$	1836	0.84
EA	EASSM	$160 \times 193 \times 160$	198	79	$0.27 \sim 32.98$	2016	1.01

Table 6.4 – Channel Flow simulations, for $Re_\tau = 2000$. MPI parallelization details. The first case has been computed with the Dynamic Smagorinsky model (DEVM) while the latter one refer to the explicit algebraic SGS model (EASSM)

Case	SGS model	n (no. processors)	N (no. nodes)	Supercomputer
DS	DEVM	40	5	Abisko
EA	EASSM	40	2	Povel

From the $\tau_w/\tau_{w,DNS}$ value we can note that the LES with DEVM strongly deviates from DNS; on the other hand, EASSM ratio agrees with DNS. Despite the resolution of the LESs is coarse, we can deduce that EASSM gives the best prediction of Re_τ.

Profiles. While in the previous simulations mean velocity profiles have been well-predicted by both EASSM and DEVM, here the difference between these two methods becomes more notable. Steady-state has been reached after $t = 800$, and EASSM gives a good prediction of the entire profile, while DEVM gives results that deviates strongly from DNS as the outer layer is approached. The good performance of EASSM is confirmed when having a look at the root-mean-squared of the streamwise, wall-normal and spanwise fluctuations. Due to an additional description of anisotropy, the EASSM is able to capture well the values of the fluctuations peaks, which are visible close to

the wall.

Like the previous $Re_\tau = 590$ case, the deviatoric part of the Reynolds stress is well predicted by both methods, however, the EASSM still gives the results closest to the DNS. The close-up of the Reynolds shear stress picture in proximity of the peak shows an important feature of the EASSM. EASSM is more successful in the peak prediction. This means that the DEVM would require a substantially better resolution for a similar result, therefore using more computational time.

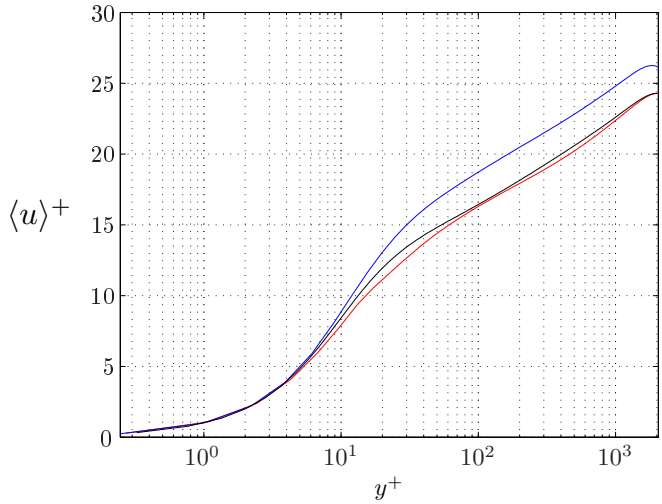

Figure 6.12 – Mean velocity profiles in wall units. – : EA – : DS0 – : DNS

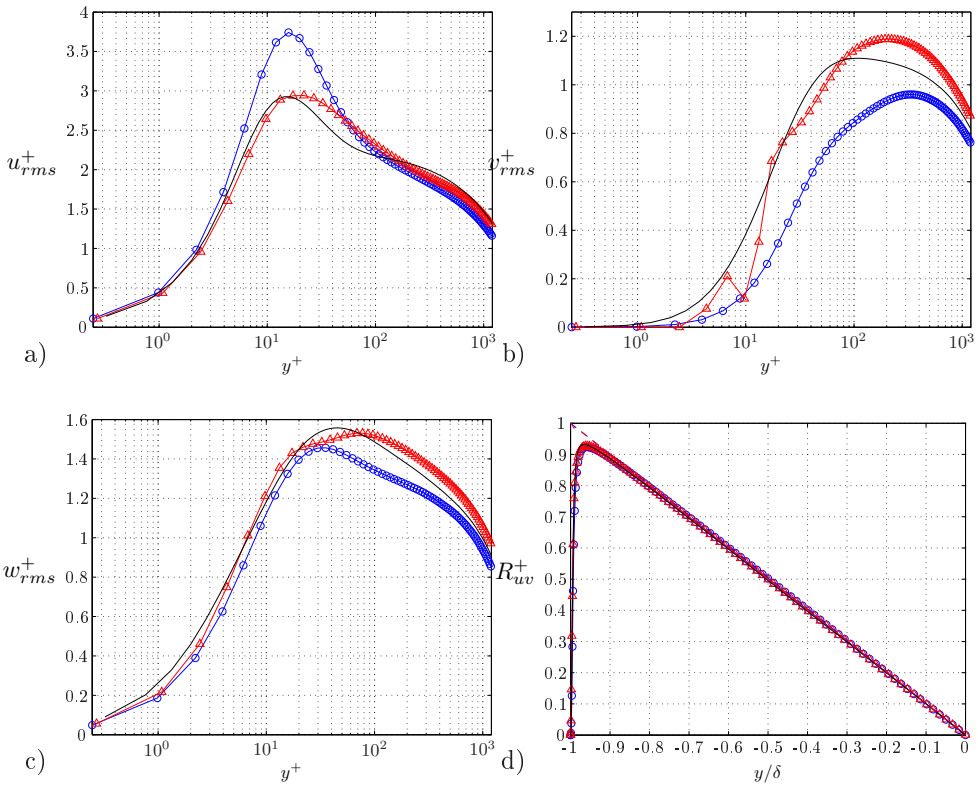

Figure 6.13 – a,b,c)Root-mean squared fluctuations in wall units, on a semilogarithmic plot d) Deviatoric part of the Reynolds stress, with total shear stress in dashed line.
– : EA, – : DS, – : DNS

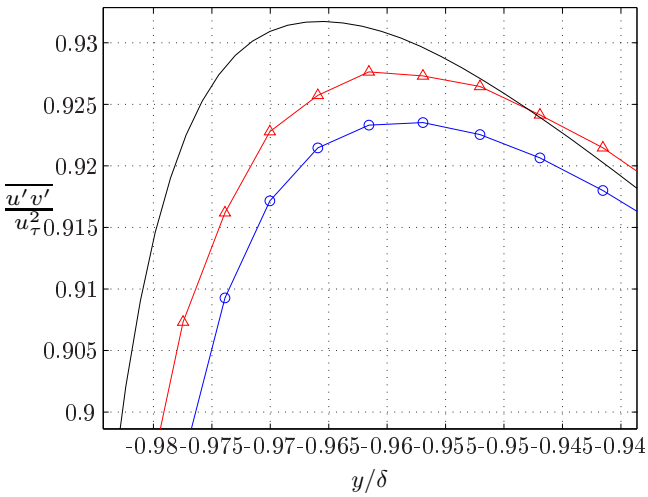

Figure 6.14 – Deviatoric part of the Reynolds stress profile in wall units. – : EA – : DS0 – : DNS

Regarding turbulent production vs dissipation ratio, we note that the DEVM underpredicts it largely, most of all in the outer region, while the explicit algebraic model shows a reasonable agreement with DNS. Results are shown in figure 6.15.

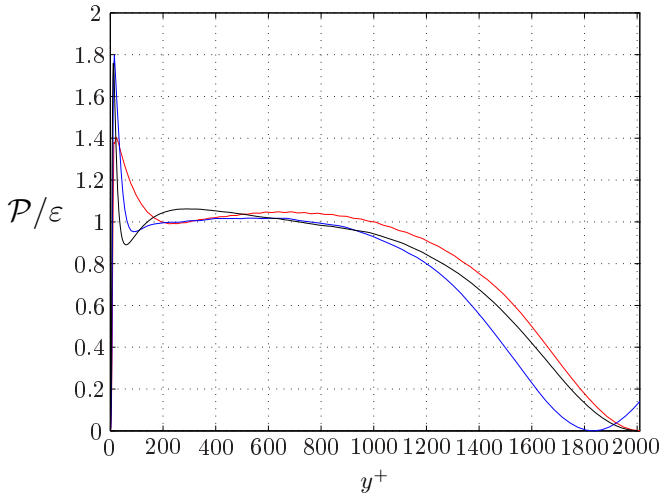

Figure 6.15 – Turbulent production-dissipation ratio. — : EA — : DS0 — : DNS

SGS Anisotropy effects. In the following diagrams the different contributions from the resolved scales and the SGS scales to the Reynolds shear stress are given, according to the definition 6.3.

Looking at the peaks (at $-1 < y/\delta < -0.9$) we can see that both models give a higher contribution of the SGS stresses, with respect to the $Re_\tau = 590$ case. It could be reasonable to expect that at higher friction Reynolds number, the bigger will be the anisotropy of the flow, most of all near the wall. For this reason the anisotropic EASSM gives the best estimation of the total Reynolds shear stress; the contribution of the SGS model is five times bigger than in the DEVM.

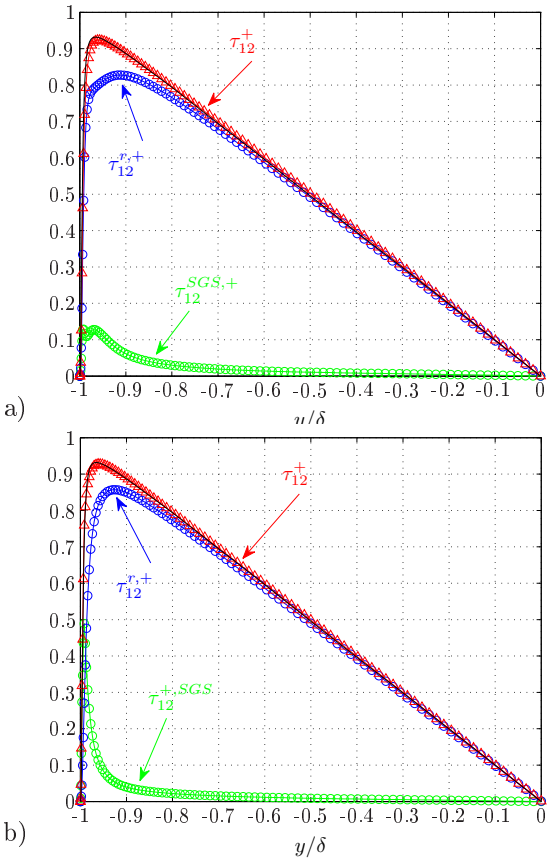

Figure 6.16 – Deviatoric part of the Reynolds stress profile in wall units, a) with DEVM model b) with EA model. Black arrows point at increasing resolutions. – : DNS

Flow visualizations. As in the previous section, some snapshots of the flow in LES, with the Explicit Algebraic (EA) and the Dynamic Smagorinsky (DS) models are presented; the snapshots have been generated at a very close distance to the wall. From a physical point of view, in this case more elongated structures are visible. This is reasonable, the higher the friction Reynolds number, the larger the total shear stress will be, with a strong contribution given by the Reynolds stress. Therefore, longer and more energetic structures will appear, than in other lower Re_τ cases.
Experimental (with particle-image velocimetry, PIV) and DNS studies have given a deeper insight of these spatially coherent, stress-bearing structures and shown that they play an important role in transport problems, particularly in the near-wall region [Marusic et al., 2010]. Therefore, in this case the accuracy of the model is investigated regarding the capability of the model to capture these elongated structures.
The EA is seen to be more able to predict these. In particular, it captures a wider range of fluctuating amplitudes, with respect to the DS model.

a)

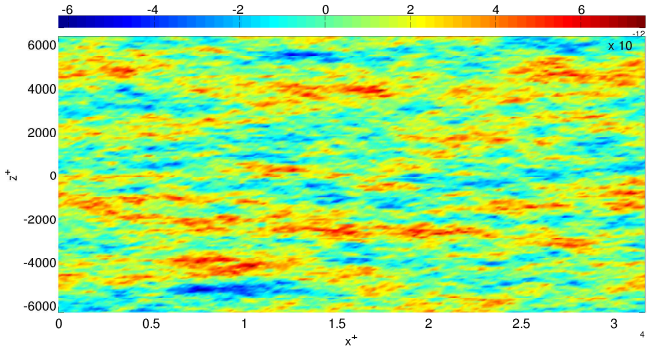

b)

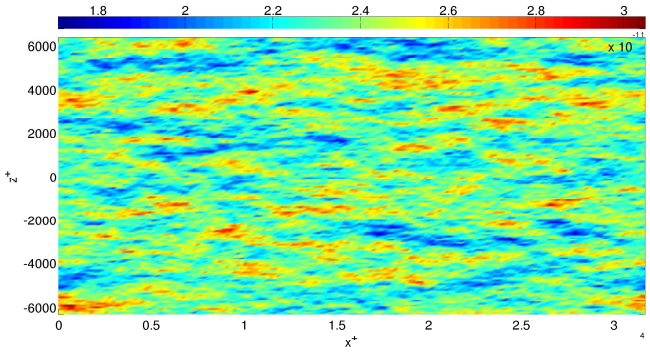

Figure 6.17 – Horizontal contour plots of streamwise fluctuations u'^+ at $y^+ \approx 8$, along the xz plane, a) simulation EA2, b) simulation DS2.

a)

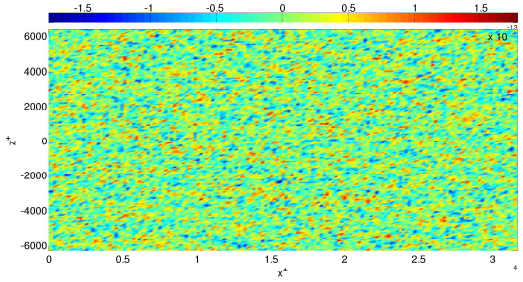

b)

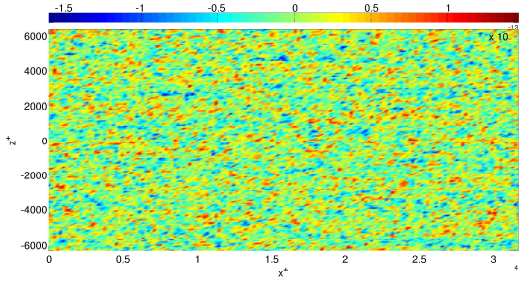

Figure 6.18 – Horizontal contour plots of wall-normal fluctuations v'^+ at $y^+ \approx 8$, along the xz plane, simulation EA2, b) simulation DS2.

a)

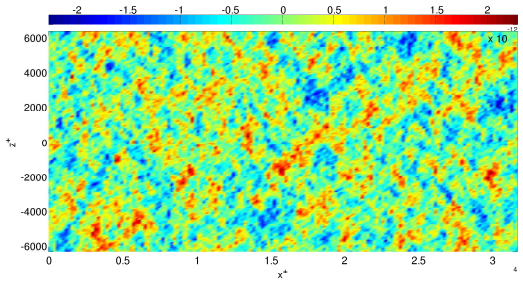

b)

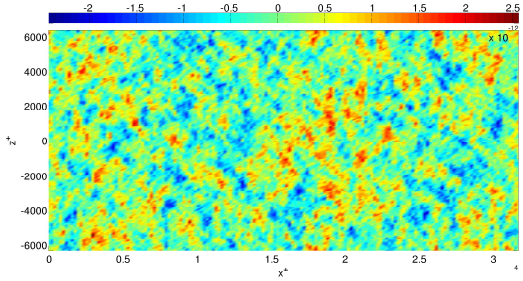

Figure 6.19 – Horizontal contour plots of spanwise fluctuations w'^+ at $y^+ \approx 8$, along the xz plane, simulation EA2, b) simulation DS2.

λ_2 structures. The accuracy of the model have also been studied by looking at the ability to predict the vorticity. Here vortical structures, computed by the *lambda method* are shown. The most significant difference between the two models concerns here the generation of vortical structures in the centerline; here the DEVM presents fewer vortical structures than the EASSM. This is a consequence given by the anisotropy estimation, since anisotropy strongly influences the flow vorticity.

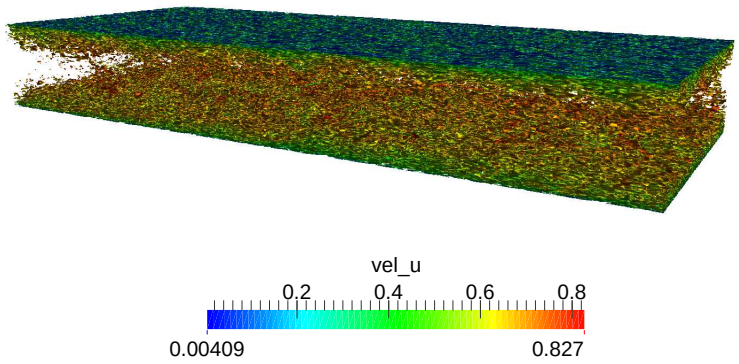

Figure 6.20 – Vortical structures in turbulent channel flow at $Re_\tau = 2000$, visualized by isosurfaces of λ_2, colored by the velocity magnitude, from EA simulation.

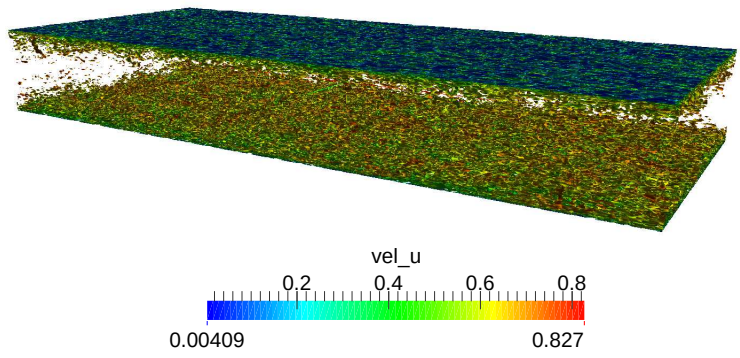

Figure 6.21 – Vortical structures in turbulent channel flow at $Re_\tau = 2000$, visualized by isosurfaces of λ_2, colored by the velocity magnitude, from DS simulation.

6.3 LES at $Re_\tau = 5200$

For this final case, we will show some results of LES, computed for the friction Reynolds number $Re_\tau = 5200$. All the results will be compared with the DNS performed by Lee & Moser (2014). Differently from the other two simulations, in the $Re_\tau = 5200$ LES with the EASSM an important issue has been faced: the previous 1D-parallelized code wasn't able to carry out simulations, because of the limited amount of processors that could be used. This problem has been solved implementing the EASSM in the SIMSON 2D parallelized code, where the work of this thesis has been focused on. Thus, it has been possible to largely extend the number of processors and, with the help of larger supercomputers, the computation has been carried out in roughly half a month.
The simulation has been carried out with a computational box $5\pi\delta$ long in streamwise direction and $2\pi\delta$ long in spanwise direction. The bulk Reynolds number is $Re_b = 128127$ and the DNS friction Reynolds number is $Re_\tau = 5186$.
Details of these simulations are shown in table 6.5.

Table 6.5 – Channel Flow LES simulation with the explicit algebraic SGS model (EASSM), at $Re_\tau = 5200$

Case	**SGS model**	$N_x \times N_y \times N_z$	Δ_x^+	Δ_z^+	$\frac{\Delta_y^+}{min \sim max}$	Re_τ	$\frac{\tau_w}{\tau_{w,DNS}}$
EA	EASSM	$512 \times 385 \times 512$	162	65	$0.17 \sim 42.54$	5293	1.04

Table 6.6 – Channel Flow simulations, for $Re_\tau = 5200$ LES with the explicit algebraic SGS model (EASSM). MPI parallelization details.

Case	**SGS model**	n (no. processors)	N (no. nodes)	Supercomputer
EA	EASSM	$16/32 \times 16/32$	11/43/64	Lindgren/Triolith

Despite the resolution is still coarse, the $\tau_w/\tau_{w,DNS}$ value shows that the Re_τ prediction with the EASSM model is very close to DNS.

Profiles. Here the good prediction of the mean velocity profile given by EASSM is even more visible in figure 6.22.The EASSM gives results that are very close to the DNS, but they begin to differ as we approach the outer layer. The underprediction by the EASSM of the outer layer can be due to convergence problems due to the limited time of the entire simulation, which is slightly small according to the previous experiences. In fact, the maximum time units reached are $t = 210$. This could indicate that the LES is not fully converged yet.

The Reynolds stress components are however well-estimated by the EASSM, apart from the fact that the u' and w' fluctuations peaks are shifted a bit in the wall-normal direction.

Reynolds stress profiles are well computed, the only exception stays in the R^+_{vv} inner layer profile [1]. Anisotropy is captured in a good way: Reynolds shear stress prediction gives only very small discrepancies, because of the limited simulation time and the not complete apparoach to the steady-state. Once more, the resolution used for the LES seems quite suitable for this friction Reynolds number.

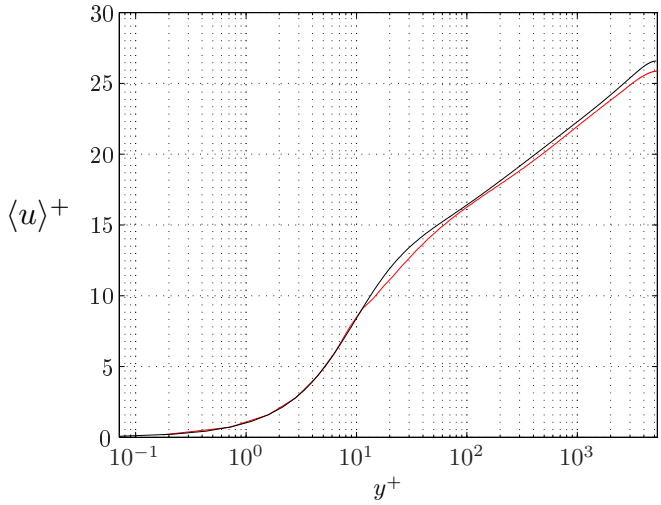

Figure 6.22 – Mean velocity profiles in wall units. – : EA – : DNS

[1] However, the misprediction of this quantity in the inner layer is due by the SGS model, and it has been proved that it doesn't influence the other results at all.

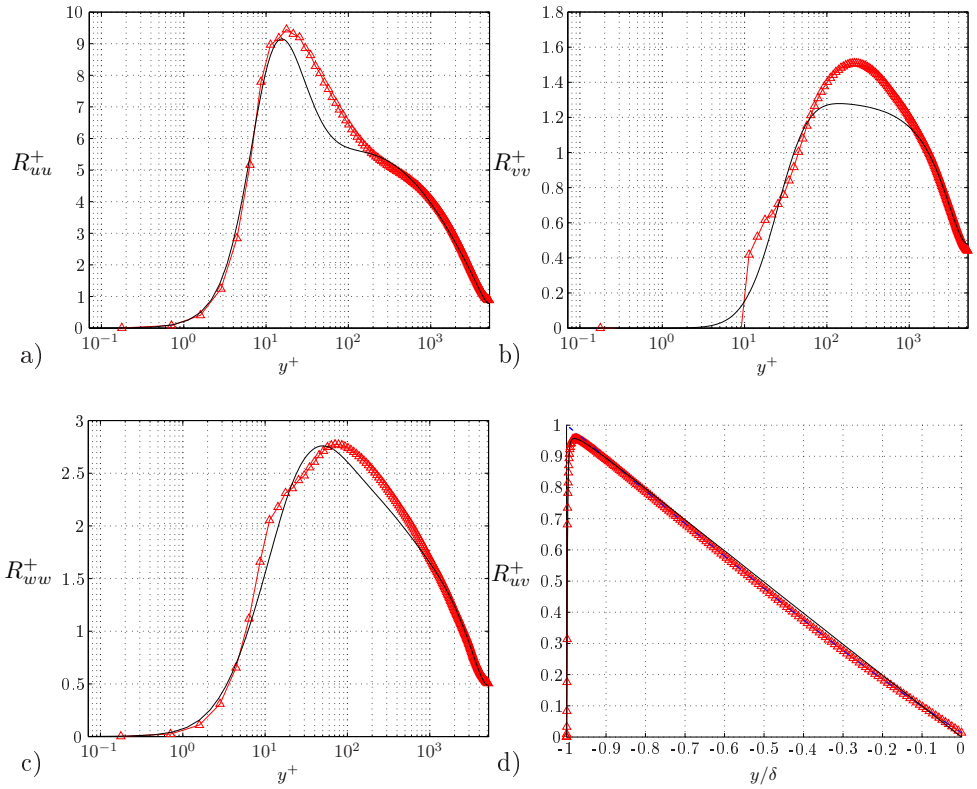

Figure 6.23 – Reynolds stress components profiles in wall units, on a semilogarithmic plot. d) Reynolds shear stress, with total shear stress in dashed line. – : EA, – : DNS

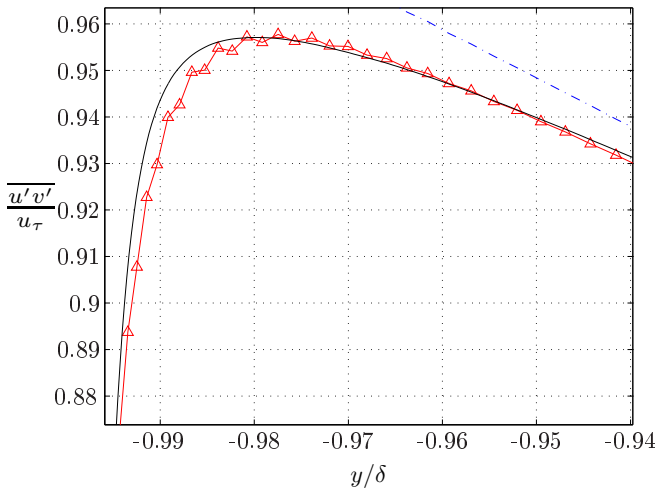

Figure 6.24 – Deviatoric part of the Reynolds stress profile in wall units. – : EA – : DNS

SGS Anisotropy effects. Let's consider only LES with EASSM. In the $Re_\tau = 590$ LES a fair and high resolution of the flow has been used so that the SGS contribution revealed to be relatively small compared to the resolved scale one. In contrast, $Re_\tau = 2000$ LES has been performed using a relatively low resolution in terms of grid spacings. As a consequence, the SGS contribution becomes significant with respect to the resolved scales. In terms of resolution, the $Re_\tau = 5200$ is an intermediate case, with grid spacings that are bigger than in the $Re_\tau = 590$ case and smaller than in the $Re_\tau = 2000$ case.
For simplicity, a reminding table with the respective grid spacings for each EASSM case is shown below.

Table 6.7 – Channel Flow simulations, for different Re_τ.

Case	SGS model	Δ_x^+	Δ_z^+	$\frac{\Delta_y^+}{min \sim max}$	Re_τ
EA2	EASSM	58	29	$0.31 \sim 19.20$	587
EA	EASSM	198	79	$0.27 \sim 32.98$	2016
EA	EASSM	162	65	$0.17 \sim 42.54$	5293

As a result, the SGS contribution is anyway notable and pushed most of all towards the wall, where it helps in the overall prediction.

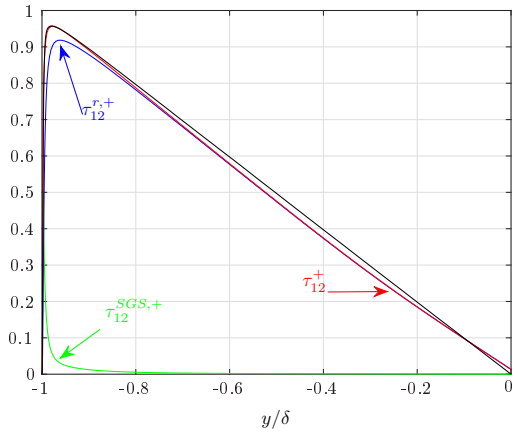

Figure 6.25 – Deviatoric part of the Reynolds stress profile in wall units, with EA model.
– : DNS

Flow visualizations. A rough resolution check can also be done by having a look at some snapshots of the flow at a very close distance from the wall. Here we can say that the resolution chosen for the streamwise and spanwise direction is right for the purpose of this simulation. Once more, some elongated structures are visible, and their length appears to be longer than in the previous cases. According to Hutchins [Hutchins and Marusic, 2007] in the near-wall region there are large-scale high-speed events, where the local istantaneous Reynolds stresses (all components: u^2,v^2,w^2 and uw) are amplified, and large low-speed events, where they are damped. This is due to the local shear rate near the wall, which is higher under high-speed events.
Regarding the resolution adopted, one may say that for the predictions of the spanwise fluctuations are accurate with a wide range of values shown.

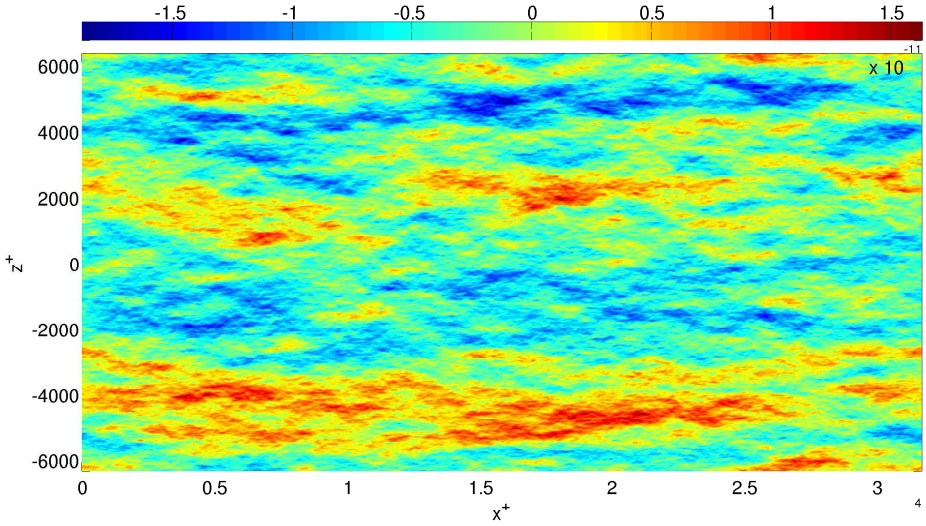

Figure 6.26 – Horizontal contour plots of streamwise u'^+ fluctuations at $y \approx -\delta$, along the xz plane, simulations EA at $Re_\tau = 5200$. The abscissa is divided by a factor of 10^{-4}.

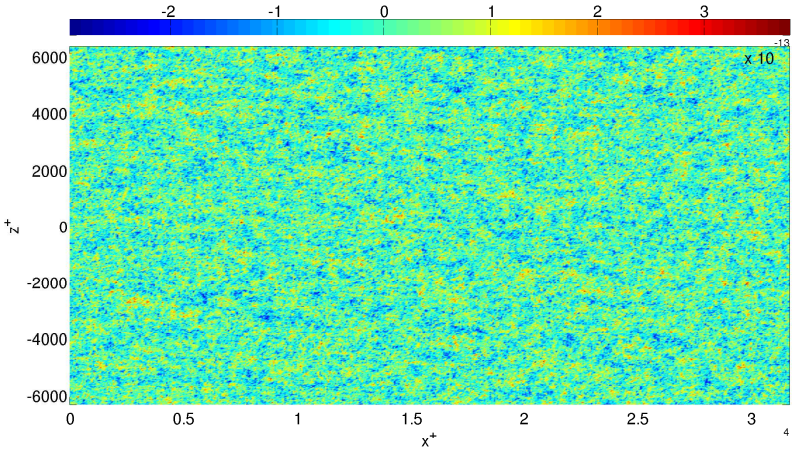

a)

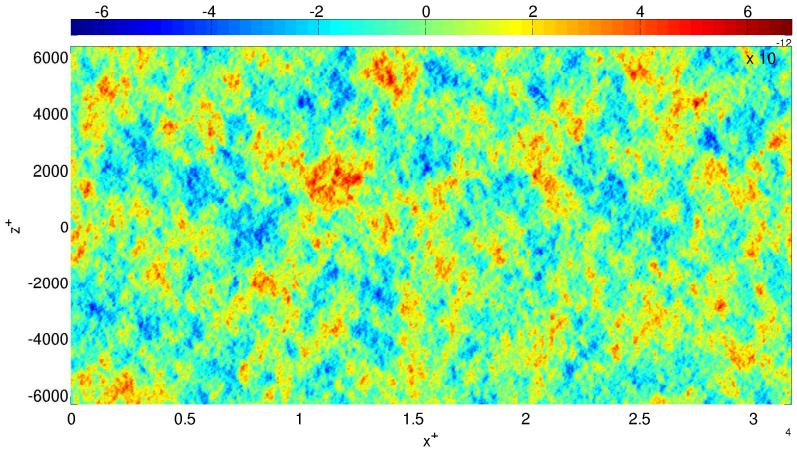

b)

Figure 6.27 – Horizontal contour plots of wall-normal v'^+ and spanwise fluctuations w'^+ at $y \approx -\delta$, along the xz plane, simulations EA at $Re_\tau = 5200$. The abscissa is divided by a factor of 10^{-4}.

λ_2 structures. For resolution reasons, this case is hard to postprocess in terms of volume renderings. Therefore, λ_2 structures for this last case are visualized only for a part of the main flow domain. In order to see how the model behaves at the wall, we have decided to reduce the domain in the following way:

$$N_x \times N_y \times N_z = 512 \times 385 \times 512 \longrightarrow 256 \times 195 \times 256$$

Vortical structures are coloured by the the velocity magnitude. The more we approach the centreline, the weaker the vortical structures will be. A possible reason to that lies in the fact that this simulation is a LES, so that the resolution adopted is not enough to completely describe the smallest scales that appears on the centreline. Therefore, LES is not able to completely capture vortical structures that are generated along the centreline.

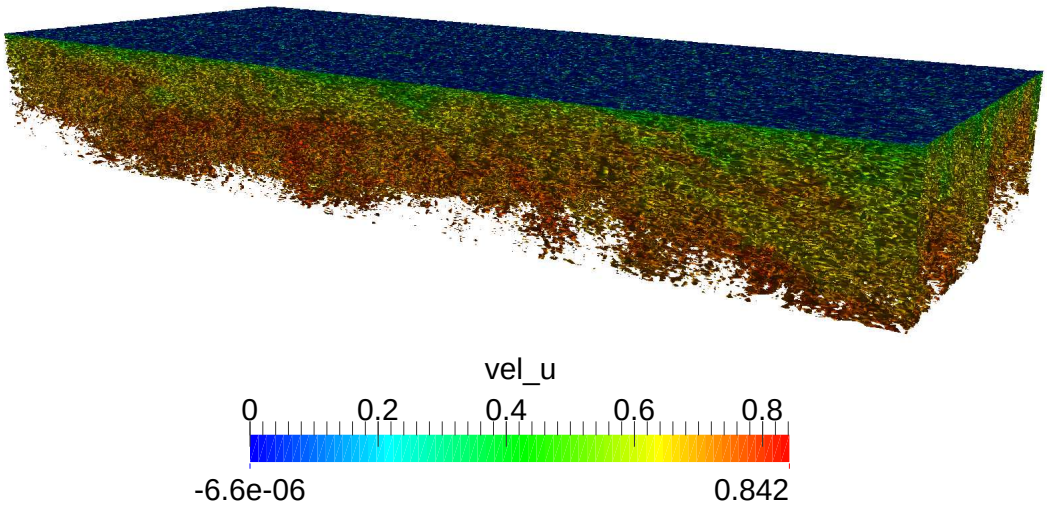

Figure 6.28 – Vortical structures in turbulent channel flow at $Re_\tau = 5200$, visualized by isosurfaces of λ_2, and coloured by the velocity magnitude, from EA simulation.

LES vs DNS: a volume perspective. To complete the analysis of the LES and the impact of EASSM on anisotropy prediction let's have an overall look to the results in terms of volume renderings of the flow. In the figures below the volume rendering of the LES with the EASSM together with the volume rendering from the DNS simulation of Lee & Moser are shown; both of them have been computed at $Re_\tau = 5200$. The resolution of the LES is high enough so that it can be compared with the DNS.

The LES is able to predict a wide range of scales, including small scales that are visible by the human eye. Apart from the smallest structures, the LES volume rendering seems of a reasonable quality and structures near the wall seem to be well-predicted.

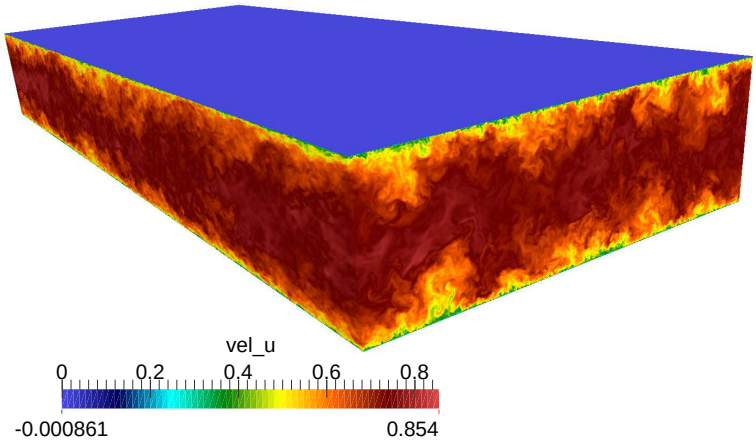

Figure 6.29 – Volume rendering of the u velocity in a turbulent channel flow at $Re_\tau = 5200$, from LES with the EASSM .

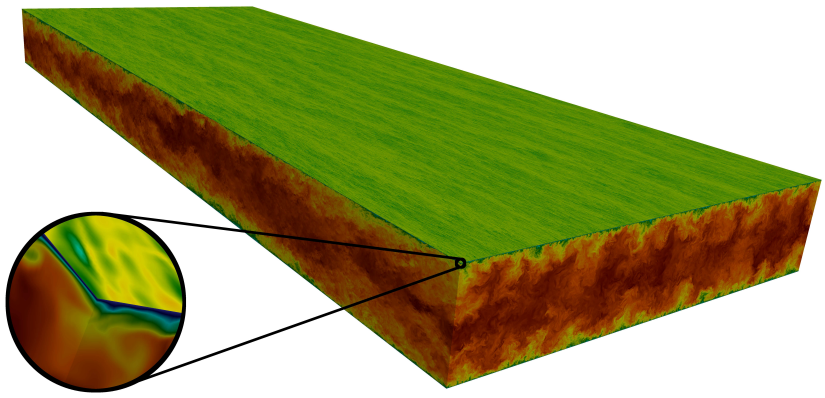

Figure 6.30 – Volume rendering of the u velocity in a turbulent channel flow at $Re_\tau = 5200$, from a DNS of Lee & Moser (2014).

High-Reynolds number reliability of the EASSM. As it was written before, EASSM is a LES model that solves an additional equation for anisotropy in order to model the SGS stress tensor. By contrast, DEVM is an eddy-viscosity based model that doesn't take into account anisotropy at all.

If we increase the friction Reynolds number anisotropic effects will become larger and larger, especially near the wall. Therefore, increasing the LES friction Reynolds number, we would expect the Explicit Algebraic model to improve the flow prediction, and the Dynamic Smagorinsky model to degrade. In order to investigate this aspect, a collection of the LES at the best resolution has been done, and a particular focus on the Reynolds shear stress has been given in figure 6.31.

For computational reasons, LES with DEVM are given only for the first two friction Reynolds numbers. The results are satisfactory and consistent with the expectations: Dynamic Smagorinsky performances become worse and worse as soon as we push the Reynolds number up to $Re_\tau = 5200$, while the EASSM get closer and closer to DNS results.

Thus, we think that with increasing Re LES with the EASSM shows better and better agreement with DNS.

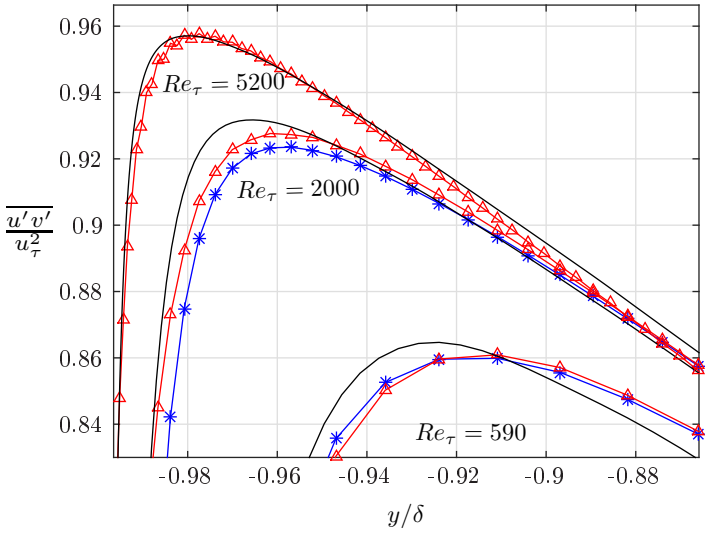

Figure 6.31 – A close-up of the Reynolds shear stress peaks very close to the wall, for three different Reynolds numbers.$-\triangle-$: EA cases, $-*-$: DEVM cases, $-$: DNS

CHAPTER

7

CONCLUSIONS & FUTURE WORK

"Towards Infinite and Beyond! (B.Lightyear)"

Large-eddy simulations of a fully developed channel flow have been performed at three different friction Reynolds numbers: $Re_\tau = 590$, $Re_\tau = 2000$ and $Re_\tau = 5200$. The first simulations, carried out for $Re_\tau = 590$, proved the capacity of the EASSM model to capture anisotropy effects of the flow. SGS contribution to the overall estimation of the flow, and in particular to the Reynolds shear stress, decreases with increasing resolutions. In contrast to the Dynamic Smagorinsky model, the averaged wall shear stress ratio of LES with the EASSM has a non-monotonic behaviour. Thus the EASSM overpredicts as well as underpredicts the wall shear stress.

EASSM has also revealed to be more accurate and suitable for high friction Reynolds number flows. The LES at $Re_\tau = 2000$ shows that the EASSM prediction of the mean flow velocity profile is much closer to the DNS results than LES with DEVM. This is a remarkable aspect most of all in the outer layer, where a big gap between DNS and LES with DEVM is noticed. A deeper study of the root-mean-squared fluctuations in x, y and z direction proves the ability of the anisotropic model to capture in a better way the peaks found close to the wall. Similar results have been obtained

for the LES with the EASSM of the last case at $Re_\tau = 5200$; EASSM behaved fairly well regarding the computation of the Reynolds stress components, especially for the Reynolds shear stress.

We have found that the gap in terms of accuracy between DEVM and EASSM becomes larger and larger at increasing friction Reynolds numbers. This is reasonable, the higher the friction Reynolds number, the more the effects of flow anisotropy are important, most of all near the wall. Therefore, EASSM is able to give a satisfactory performance also at high Re_τ, while the DEVM gives get worse and worse predictions.

Another important aspect is that a considerable reduction of computational resources is possible using the EASSM. The accuracy achieved with a coarser mesh is comparable only to a DEVM case with a fine mesh. The coarser the mesh, the lower the computational time needed to run the simulation.

In this thesis work, only *non-rotating flows*, are investigated. However, the EASSM is also very suitable for LES of rotating flows, e.g. rotating channel flows. A possible continuation of this work would be a complete study of LES of rotating channel flows with separation cases and the investigation of the behaviour of the Explicit Algebraic SGS Scalar Flux (EASFM), for the case at $Re_\tau = 5200$ and beyond. Complex geometries will also be taken into account in further studies.

The work will be continued with a PhD work in LES modelling at KTH, in order to present the results at the European Turbulence Conference 15 (ETC15) where the simulation results with the Explicit Algebraic SGS model at $Re_\tau = 5200$ will be compared with the performances of the Dynamic Smagorinsky model, together with DNS data as reference.

The simulation time will be increased using a more powerful supercomputer, in order to reach a fully developed steady state of the flow.

BIBLIOGRAPHY

[Boyd, 2001] Boyd, J. P. (2001). *Chebyshev and Fourier spectral methods*. Courier Corporation.

[Chevalier et al., 2007] Chevalier, M., Schlatter, P., Lundbladh, A., and Henningson, D. S. (2007). Simson: A pseudo-spectral solver for incompressible boundary layer flows.

[Choi and Moin, 2012] Choi, H. and Moin, P. (2012). Grid-point requirements for large eddy simulation: Chapman's estimates revisited. *Physics of Fluids (1994-present)*, 24(1):011702.

[Chow and Moin, 2003] Chow, F. K. and Moin, P. (2003). A further study of numerical errors in large-eddy simulations. *Journal of Computational Physics*, 184(2):366–380.

[Daly and Harlow, 1970] Daly, B. J. and Harlow, F. H. (1970). Transport equations in turbulence. *Physics of Fluids (1958-1988)*, 13(11):2634–2649.

[Gatski and Speziale, 1993] Gatski, T. and Speziale, C. G. (1993). On explicit algebraic stress models for complex turbulent flows. *Journal of Fluid Mechanics*, 254:59–78.

[Germano et al., 1991] Germano, M., Piomelli, U., Moin, P., and Cabot, W. H. (1991). A dynamic subgrid-scale eddy viscosity model. *Physics of Fluids A: Fluid Dynamics (1989-1993)*, 3(7):1760–1765.

[Geurts and Fröhlich, 2002] Geurts, B. J. and Fröhlich, J. (2002). A framework for predicting accuracy limitations in large-eddy simulation. *Physics of Fluids (1994-present)*, 14(6):L41–L44.

[Ghosal, 1996] Ghosal, S. (1996). An analysis of numerical errors in large-eddy simulations of turbulence. *Journal of Computational Physics*, 125(1):187–206.

[Gropp et al., 1999] Gropp, W., Lusk, E., and Skjellum, A. (1999). *Using MPI: portable parallel programming with the message-passing interface*, volume 1. MIT press.

[Hutchins and Marusic, 2007] Hutchins, N. and Marusic, I. (2007). Large-scale influences in near-wall turbulence. *Philosophical Transactions of the Royal Society A: Mathematical, Physical and Engineering Sciences*, 365(1852):647–664.

[Jeong and Hussain, 1995] Jeong, J. and Hussain, F. (1995). On the identification of a vortex. *Journal of fluid mechanics*, 285:69–94.

[Johansson and Wallin, 2012] Johansson, A. and Wallin, S. (2012). *Turbulence Lecture notes*. KTH, Royal Institute of Technology.

[Kim, 1988] Kim, C. (1988). A two-equation model for heat transport in wall turbulent shear flows. *Journal of heat transfer*, 110:583.

[Kravchenko et al., 1996] Kravchenko, A., Moin, P., and Moser, R. (1996). Zonal embedded grids for numerical simulations of wall-bounded turbulent flows. *Journal of Computational Physics*, 127(2):412–423.

[Launder et al., 1975] Launder, B., Reece, G. J., and Rodi, W. (1975). Progress in the development of a reynolds-stress turbulence closure. *Journal of fluid mechanics*, 68(03):537–566.

[Laure, 2014] Laure, E. (2014). Writing parallel applications using mpi. KTH, Royal Institute of Technology.

[Lee and Moser, 2014] Lee, M. and Moser, R. D. (2014). Direct numerical simulation of turbulent channel flow up to retau = 5200. *Journal of Fluid Mechanics (Submitted)*.

[Leonard, 1974] Leonard, A. (1974). Energy cascade in large-eddy simulations of turbulent fluid flows. In *Turbulent Diffusion in Environmental Pollution*, volume 1, pages 237–248.

[Lund and Novikov, 1993] Lund, T. S. and Novikov, E. (1993). Parameterization of subgrid-scale stress by the velocity gradient tensor.

[Marstorp et al., 2009] Marstorp, L., Brethouwer, G., Grundestam, O., and Johansson, A. V. (2009). Explicit algebraic subgrid stress models with application to rotating channel flow. *Journal of Fluid Mechanics*, 639:403–432.

[Marusic et al., 2010] Marusic, I., McKeon, B., Monkewitz, P., Nagib, H., Smits, A., and Sreenivasan, K. (2010). Wall-bounded turbulent flows at high reynolds numbers: Recent advances and key issues. *Physics of Fluids (1994-present)*, 22(6):065103.

[McDonough, 2007] McDonough, J. M. (2004,2007). *INTRODUCTORY LECTURES on TURBULENCE: Physics, Mathematics and Modeling*. Departments of Mechanical Engineering and Mathematics, University of Kentucky.

[Menter, 1994] Menter, F. R. (1994). Two-equation eddy-viscosity turbulence models for engineering applications. *AIAA journal*, 32(8):1598–1605.

[Moin et al., 1991] Moin, P. a., Squires, K., Cabot, W., and Lee, S. (1991). A dynamic subgrid-scale model for compressible turbulence and scalar transport. *Physics of Fluids A: Fluid Dynamics (1989-1993)*, 3(11):2746–2757.

[Pope, 1975] Pope, S. (1975). A more general effective-viscosity hypothesis. *Journal of Fluid Mechanics*, 72(02):331–340.

[Pope, 2000] Pope, S. B. (2000). *Turbulent flows*. Cambridge university press.

[Rasam, 2014] Rasam, A. (2014). *Anisotropy-resolving subgrid-scale modelling using explicit algebraic closures for large eddy simulation*. PhD thesis, KTH, Royal Institute of Technology.

[Rasam et al., 2011] Rasam, A., Brethouwer, G., Schlatter, P., Li, Q., and Johansson, A. V. (2011). Effects of modelling, resolution and anisotropy of subgrid-scales on large eddy simulations of channel flow. *Journal of turbulence*, (12).

[Reynolds, 1894] Reynolds, O. (1894). On the dynamical theory of incompressible viscous fluids and the determination of the criterion. *Proceedings of the Royal Society of London*, 56(336-339):40–45.

[Rodi, 1992] Rodi, W. (1992). *The prediction of free turbulent boundary layers by use of a two-equation model of turbulence*. PhD thesis, Imperial College London (University of London).

[Smagorinsky, 1963] Smagorinsky, J. (1963). General circulation experiments with the primitive equations: I. the basic experiment*. *Monthly weather review*, 91(3):99–164.

[Spalart, 2015] Spalart, P. R. (2015). Philosophies and fallacies in turbulence modeling. *Progress in Aerospace Sciences*.

[Spalart and Allmaras, 1992] Spalart, P. R. and Allmaras, S. R. (1992). A one-equation turbulence model for aerodynamic flows.

[Sreenivasan, 1995] Sreenivasan, K. R. (1995). On the universality of the kolmogorov constant. *Physics of Fluids (1994-present)*, 7(11):2778–2784.

[Talamelli et al., 2009] Talamelli, A., Persiani, F., Fransson, J. H., Alfredsson, P. H., Johansson, A. V., Nagib, H. M., Rüedi, J.-D., Sreenivasan, K. R., and Monkewitz, P. A. (2009). Ciclope - a response to the need for high reynolds number experiments. *Fluid dynamics research*, 41(2):021407.

[Taylor, 1915] Taylor, G. I. (1915). Eddy motion in the atmosphere. *Philosophical Transactions of the Royal Society of London. Series A, Containing Papers of a Mathematical or Physical Character*, pages 1–26.

[Wallin and Johansson, 2000] Wallin, S. and Johansson, A. V. (2000). An explicit algebraic reynolds stress model for incompressible and compressible turbulent flows. *Journal of Fluid Mechanics*, 403:89–132.

[Wang and Bergstrom, 2005] Wang, B.-C. and Bergstrom, D. J. (2005). A dynamic nonlinear subgrid-scale stress model. *Physics of Fluids (1994-present)*, 17(3):035109.

[Yoshizawa, 1986] Yoshizawa, A. (1986). Statistical theory for compressible turbulent shear flows, with the application to subgrid modeling. *Physics of Fluids (1958-1988)*, 29(7):2152–2164.

ACKNOWLEDGEMENTS - RINGRAZIAMENTI

My best acknowledgements are for prof. Arne Johansson, who gave me the chance to work in a very recent and innovative project. Dr. Geert Brethouwer is strongly acknowledged for the full revision of my thesis and for giving me lots of important and useful tips in scientific computing for turbulence.

Computer time allocation provided by the Swedish National Infrastructure for Computing (SNIC) is gratefully acknowledged.

La mia gratitudine va anche al prof. Alessandro Talamelli per la sua fiducia in me, dandomi la grande possibilitá di venire qui al KTH a Stoccolma, e di seguirmi per tutto il mio percorso accademico.

Sono convinto che ognuno di noi sia il risultato dell'esperienza che ogni giorno vive. Senza dubbio, non posso negare che i quattro anni vissuti a Forlí siano stati decisivi per la mia crescita interiore e rimarranno sempre nel mio cuore.

Da ragazzo appena uscito da una realtá minuscola come Camerino, ricordo ancora le prime persone che ho conosciuto, che mi hanno sostenuto durante il mio impegnativo percorso universitario. In primis vorrei inondare di ringraziamenti coloro che hanno condiviso con me e piu da vicino questi

anni, il leggendario Appa Matteotti : Adel, Sabba, Otta, il buon Danilo, Andre, Matte e anche Spock, vi sono debitore per tutte quelle volte che siete riusciti a farmi sorridere e divertire! Non avrei potuto chiedere di meglio, *la vostra amicizia e una delle cose piú preziose che la vita mi ha donato*. Grazie.

Fra, Mita, Winx e Ara: anche se non ci siamo sentiti spesso durante la mia permanenza svedese, ricordare la vostra compagnia, le *lunghe giornate di studio insieme* e i *tanti discorsi* fatti mi riempie di felicitá.

Un grazie particolare va anche a Michele, ci terrei ad evidenziare come questi due sprovveduti Camerinesi si siano fatti largo e siano riusciti entrambi a laurearsi in cosi poco tempo. Le tue forti motivazioni durante il primo anno di Universitá (e successivi, nonostante vivessimo in 2 appartamenti differenti) sono state essenziali per acquistare la fiducia in me stesso e superare anche gli esami piu difficili.

Voglio anche ringraziare i miei *motivatori* e *compagni di vita* in Svezia, i carissimi Domenico, Walter e Matteo. Siamo stati compagni di corso e di vita, abbiamo condiviso cosi' tanto che non basterebbe un'intera tesi per raccontare le nostre avventure.

Infine, un grazie, impossibile da definire nelle dimensioni, va alla mia famiglia. Mamma e Babbo, spero di essere riuscito almeno a ripagarvi dei vostri sacrifici con qualche soddisfazione. Il vostro appoggio morale, la *grande fiducia* che avete riposto in me nei *momenti piú decisivi* del mio percorso scientifico, mi lascia commosso. Vi sono grato per tutte le *esperienze* che mi avete donato, poiché ciascuna di esse hanno contribuito a farmi diventare la persona che sono ora.

Marco, spero che questo piccolo lavoro di tesi sia una dimostrazione per te che *con la buona volontá e la passione si puó raggiungere qualsiasi obiettivo*. Non permettere mai a nessuno di dirti che non sai fare qualcosa, neanche a me. Se hai un sogno, tu lo devi proteggere. Se vuoi qualcosa...vai lí e inseguila!

Un grazie anche *a chi non si é limitato fisicamente* ad assistere alla mia discussione, ma che sta vedendo i miei progressi giorno dopo giorno dal Cielo. Spero almeno che tu ti sia compiaciuto di quello che sono riuscito a combinare.

Matteo Montecchia
Stockholm, February 2015